
QUASI-ORTHOGONAL FOLIATIONS OF THE CONFIGURATION SPACE – A REDUNDANCY RESOLUTION APPROACH AT POSITION LEVEL

A PREPRINT

 **Alin Albu-Schäffer**

Institute of Robotics and Mechatronics
German Aerospace Center (DLR)
Oberpfaffenhofen, Germany
alin.albu-schaeffer@dlr.de

 **Arne Sachtler**

Department of Informatics
Technical University of Munich (TUM)
Garching, Germany
arne.sachtler@dlr.de

April 25, 2022

ABSTRACT

High versatility and flexibility of robotic systems require kinematic structures with many degrees of freedom. This usually renders the system kinematically redundant, i.e., its maneuvers are not fully determined by the main manipulation or interaction task. Additional constraints or objectives are required to solve the under-determined control and planning problems. The state of the art approaches involve arranging tasks in a hierarchy and decoupling lower from higher priority tasks on velocity or torque level. Velocities and torques are elements of vector and covector spaces, respectively, and thus the approaches are inherently based on linear algebra tools. In this paper we develop an approach to redundancy resolution and decoupling on position level. That requires moving from vector spaces and linear algebra to manifolds and differential geometry. We propose to determine, in addition to the task forward kinematics, another set of coordinate functions. The Jacobian of those functions shall resemble the conditions known from the linear algebra based velocity- and torque-level decoupling to the best extent possible. The approach provides a better insight into the topological properties of robot kinematics and control problems, allowing a more global geometrical view. Quasi-decoupled coordinates can help to avoid or diminish some practical and theoretical difficulties related to the classical projection approaches at the cost of higher offline computational efforts. A condition for the existence of these coordinates is derived. If the condition is not satisfied, one can still find approximate solutions by numerical optimization. Finally, we show simulation results for both, trajectory tracking and classical impedance control.

Keywords redundancy resolution, redundant robots, impedance control, decoupling, dynamical decoupling, neural networks

1 Introduction

Kinematics and dynamics of redundant robots belong to the classical and most well-studied theoretical foundations of robotics [Kha87, Kha95, NHY87, SS91, NCM⁺08, BB98, HK87, Sic90, DOAS13]. The state of the art is comprehensively presented in [SK08], as well as in the standard literature [SSVO09, MSZ94, LP17, SHV05]. The basics of redundancy resolution are summarized below for convenience.

We denote the forward kinematics mapping for two task priorities between the configuration (joint) space \mathcal{Q} and the task space \mathcal{M}_i by $\mathbf{h}_i : \mathcal{Q} \rightarrow \mathcal{M}_i$. Local coordinates for \mathcal{Q} are denoted by $\mathbf{q} \in \mathbb{R}^n$ while $\mathbf{x}_i \in \mathbb{R}^{m_i}$, $i = \{1, 2\}$, $m_1 + m_2 \leq n$ are local coordinates for two levels of task priorities, where task 1 is higher in priority than task 2. The associated Jacobians are $\mathbf{J}_i = \frac{\partial \mathbf{h}_i(\mathbf{q})}{\partial \mathbf{q}}$.

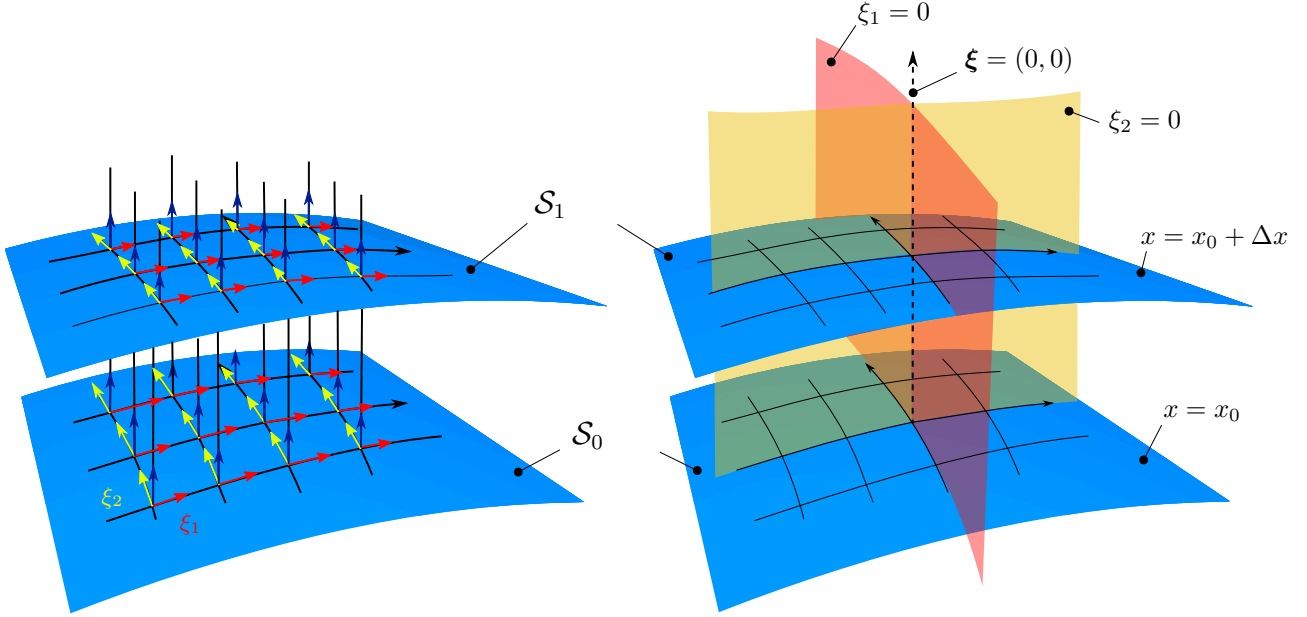


Figure 1: The idea of orthogonal foliations (and coordinates): given the foliation induced by the forward kinematics of a redundant manipulator, we assign coordinates (ξ_1, ξ_2) on the self-motion motion manifolds (denoted in blue), such that the coordinates remain invariant when moving to another leaf of the foliation by following the task gradient (i.e the Jacobian in the kinematic case). This leads to foliations that are orthogonal to the task-induced foliation in the sense of a specified metric. Two leaves of the orthogonal foliations are shown in red and yellow.

While the higher priority task is usually some specification of the manipulation task performed with the end-effector, the lower priority often optimizes kinematic or dynamic properties of the robot. These objectives are formulated as functions of the configurations variables, usually being some kind of thresholded inverse distance functions for (self) collision avoidance [Kha85, MK85, DWAH12, HKT⁺09], values required to optimize manipulability [HOW14, SLM⁺19] or inertial properties [Wal90, MDV⁺17].

The classical redundancy resolution on velocity level [NHY87, SS91, NCM⁺08, BB98] at non-singular configurations $(\det(\mathbf{J}_1(\mathbf{q})\mathbf{J}_1^\top(\mathbf{q})) \neq 0)$ imposes the following relations between task and joint space velocities

$$\dot{\mathbf{q}} = \mathbf{J}_1^\#(\mathbf{q})\dot{\mathbf{x}}_1 + \dot{\mathbf{q}}_N \quad (1a)$$

$$\dot{\mathbf{q}}_N = \mathbf{P}(\mathbf{q})\mathbf{J}_2^\#(\mathbf{q})\dot{\mathbf{x}}_2. \quad (1b)$$

Therein, $\dot{\mathbf{q}}_N$ are null space velocities, $\#$ denotes a pseudo-inverse and $\mathbf{P}(\mathbf{q})$ is a projector onto the null space of \mathbf{J}_1 defined as

$$\mathbf{P}(\mathbf{q}) = \mathbf{I} - \mathbf{J}_1^{\#A}(\mathbf{q})\mathbf{J}_1(\mathbf{q}), \quad (2)$$

with $\mathbf{J}_1^{\#A} = \mathbf{A}^{-1}\mathbf{J}_1^\top(\mathbf{J}_1\mathbf{A}^{-1}\mathbf{J}_1^\top)^{-1}$ being the generalized pseudo-inverse w.r.t. the positive definite and symmetric metric tensor \mathbf{A} [DMB93]. It satisfies $\mathbf{J}_1(\mathbf{q})\mathbf{P}(\mathbf{q}) = \mathbf{0}$ and thus ensures $\mathbf{J}_1(\mathbf{q})\dot{\mathbf{q}}_N = \mathbf{0}$. The columns of $\mathbf{P}(\mathbf{q})$ form a basis for the null space $\ker(\mathbf{J}_1(\mathbf{q}))$ of the Jacobian $\mathbf{J}_1(\mathbf{q})$.

Similarly, in the framework of operational space control [Kha87], redundancy resolution of the generalized joint force $\boldsymbol{\tau}$ considering primary and secondary task forces \mathbf{f}_1 and \mathbf{f}_2 , respectively, is obtained according to

$$\boldsymbol{\tau} = \mathbf{J}_1^\top(\mathbf{q})\mathbf{f}_1 + \boldsymbol{\tau}_N \quad (3a)$$

$$\boldsymbol{\tau}_N = \mathbf{P}^\top(\mathbf{q})\mathbf{J}_2^\top(\mathbf{q})\mathbf{f}_2. \quad (3b)$$

Since the projector satisfies $\mathbf{P}^\top(\mathbf{q})\mathbf{J}_1^\top(\mathbf{q})\mathbf{f}_1 = \mathbf{0}$, it removes any generalized joint force component, which would interfere with the one generated by a primary task force \mathbf{f}_1 over the Jacobian $\mathbf{J}_1^\top(\mathbf{q})$. Using the inertia tensor for the metric in the pseudo-inverse, i.e., $\mathbf{A} = \mathbf{M}(\mathbf{q})$, one obtains the dynamically decoupled projection, additionally satisfying the condition that, instantaneously, no primary task acceleration $\ddot{\mathbf{x}}_1$ is generated by $\boldsymbol{\tau}_N$ [Kha87].

It is not accidental that the state of the art redundancy resolution methods are formulated at the level of velocities $\dot{\mathbf{q}}$ or generalized forces $\boldsymbol{\tau}$. For any given robot configuration \mathbf{q} these two quantities are elements of linear vector spaces.

Thus linear algebra and the associated powerful numerical methods can be directly applied. These are currently the only available types of approaches allowing efficient real-time implementation for robot control.

For many applications in control and motion planning it would be, however, desirable to have a set of configuration coordinates $\xi(\mathbf{q})$ such that their Jacobian $\mathbf{J}_\xi(\mathbf{q}) = \frac{\partial \xi(\mathbf{q})}{\partial \mathbf{q}}$ forms a basis of the null space of $\mathbf{J}_1(\mathbf{q})$, thus fulfilling $\mathbf{J}_1(\mathbf{q})\mathbf{J}_\xi^\top(\mathbf{q}) = \mathbf{0}$ or $\mathbf{J}_1(\mathbf{q})\mathbf{M}^{-1}\mathbf{J}_\xi^\top(\mathbf{q}) = \mathbf{0}$, depending on the desired properties of the coordinates. Such a redundancy resolution at configuration level, based on coordinates for the self-motion manifolds, would provide a more global perspective, which is not limited to the linearized vicinity of the current configuration.

Constructing a null space basis $\mathbf{J}_{\xi'}(\mathbf{q})$ independently of an integral manifold $\xi(\mathbf{q})$, i.e., purely based on linear algebra, is of course always possible and has been frequently addressed in the literature [PCY99, OKN08, DOAS15, Sic90]. Performing a null space projection based on (1b) or (3b) can be equivalently formulated using the null space basis, see Sec. 3.2. However, it is well-known [KH83] that the velocity vector fields obtained by the projector $\mathbf{P}(\mathbf{q})$ in (1b), and equivalently, obtained by $\dot{\xi}' = \mathbf{J}_{\xi'}(\mathbf{q})\dot{\mathbf{q}}$, are in general not integrable, not fulfilling the conditions of the Frobenius theorem [Fro77]. For example, performing a loop and returning to the same robot joint configuration $\mathbf{q}(t_0) = \mathbf{q}(t_1)$ does not lead in general to a zero time integral of the null space velocities. So, when defining $\xi'(t_1) = \xi'(t_0) + \int_{t_0}^{t_1} \dot{\xi}'(\tau) d\tau$ one would in general have $\xi'(t_1) \neq \xi'(t_0)$, i.e. ξ' is not a function of \mathbf{q} only, but also depends on the path taken to reach \mathbf{q} , i.e., the system is nonholonomic w.r.t. ξ' .

The present paper provides an alternative approach, imposing integrability as a constraint and identifying appropriate null space bases in an optimization approach. We start with a parametrized function and then optimize the parameters to achieve orthogonality of the Jacobians.

Passivity-based multi-layer control approaches generate the task forces in (3a), (3b) as gradient force fields $\mathbf{f}_i^\top = \frac{\partial U_i(\mathbf{x}_i)}{\partial \mathbf{x}_i}$, $i = 1, 2$, derived from potential fields U_i formulated in task coordinates \mathbf{x}_i . Through the null space projection of the secondary layer force \mathbf{f}_2 , however, the resulting generalized force τ_N will generally not be integrable either. Providing effective dynamical decoupling and proving convergence under these conditions is a complex challenge, still a topic of active research today [DOAS15, DWAH12]. This is especially true regarding the realization of task coordinates, which are structurally feasible. In general, it is hard to guarantee that the tasks resulting from various robot specifications do not interfere for the entire robot motion as the methods are inherently local. In most null space projection-based controllers, the assumption of structural feasibility of the task coordinates is made [DO20] and this problem is deferred to a planning task. In this work, we will give explicit mathematical formulations and intuitive discussions of the globally available configuration space on a lower priority level given the description of high level tasks. Moreover, we give an explicit way of parametrizing this space and optimize decoupling. Defining the secondary level potential based on the redundancy resolution coordinates $\xi(\mathbf{q})$ mentioned above will provide an interesting alternative approach.

We therefore address the question of generalized configuration coordinates, which are orthogonal to given high-priority task coordinates. This requires moving from vector spaces and linear algebra to smooth manifolds and the tools of differential geometry and topology. The first differential geometry based analysis of redundant robots goes back to [Bur89], who introduced the notion of self-motion manifolds to robotics. A comprehensive differential geometric treatment of robot kinematics and dynamics was given in [MSZ94, Sel96] and has been since then constantly used in robotics [PBP95, PK98, MIH91], although not yet belonging to the standard, widely used repertoire. Additionally, there is a close connection between the dynamics of conservative mechanical systems and Riemannian manifolds [DCGP19]. These are two reasons why we think that a differential geometric approach of the problem, attacking the solution of nonlinear equations and nonlinear differential equations makes sense today. First, computational resources and methods for numerical nonlinear system approximation, including neural networks, witnessed a major progress in the last decade, due to efficient optimization/training software and specialized hardware such as GPU clusters. Secondly, new results in mathematics, which help to address the posed question in an adequate way, become increasingly accessible to the robotics community.

As it will turn out in the paper, integrability cannot be exactly achieved in the general case. We will therefore discuss the cases in which integrability can be ensured. If this is not the case, our proposed learning method will provide coordinates that are "as orthogonal as possible" in a certain optimization sense. Examples will be provided in both cases.

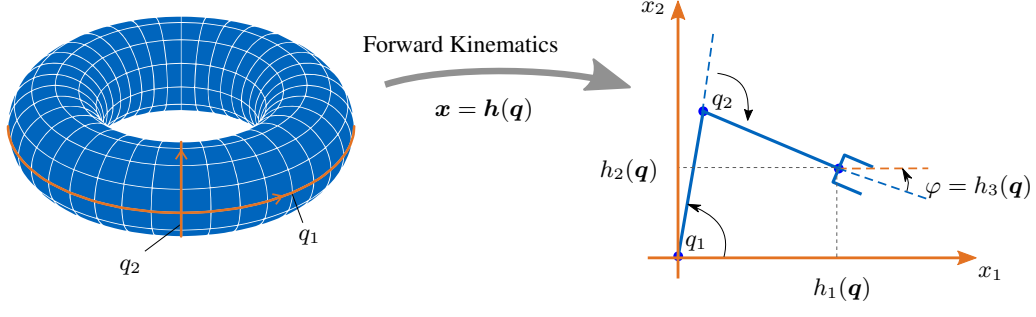


Figure 2: The forward kinematics is a mapping between the joint manifold \mathcal{Q} and the task manifold \mathcal{M} . The task space manifold in this example is $\mathcal{M} = SE(2)$, which we sketch in a coordinate representation on the right.

2 Redundant Robots in Light of Differential Geometry

As in the introduction, let \mathcal{Q} denote the configuration space manifold of a robot and \mathcal{M} the task space manifold. We call $\mathcal{H} : \mathcal{Q} \rightarrow \mathcal{M}$ the forward kinematics map. Further, let $n = \dim \mathcal{Q}$ and $m = \dim \mathcal{M}$. A robot will be called redundant for a certain task if $m < n$ [Kha95]. Obviously, being redundant is not only dependent on the degrees of freedom of the robot. Statements on the kinematic redundancy of a robot can only be made given the kinematic structure and a choice of a task space. When considering for example $\mathcal{M} = SE(2)$ or $\mathcal{M} = SE(3)$ as task manifolds, this is precisely the case when $n > 3$ or $n > 6$, respectively.

Of course, for describing the task manifold, various local coordinates can be chosen, as highlighted in [MSZ94] for the representation of orientations. The same is true for the configuration space manifold \mathcal{Q} . Especially when ball joints are part of the mechanism the same issues concerning the representation of orientations arise. However, following a differential geometric perspective, most statements will be defined in a coordinate-invariant way.

We denote local coordinates of a point in \mathcal{Q} by $\mathbf{q} \in \mathbb{R}^n$ and local coordinates for a point in \mathcal{M} by $\mathbf{x} \in \mathbb{R}^m$. In coordinates the mapping \mathcal{H} will be denoted $\mathbf{h} : \mathbb{R}^n \rightarrow \mathbb{R}^m$ such that $\mathbf{x} = \mathbf{h}(\mathbf{q})$. Fig. 2 shows an example of such a mapping. We will use a fair amount of abuse of notation in this paper: By \mathbf{q}/\mathbf{x} we refer to both, a point $\mathbf{q} \in \mathcal{Q}/\mathbf{x} \in \mathcal{M}$ and to its coordinates $\mathbf{q} \in \mathbb{R}^n/\mathbf{x} \in \mathbb{R}^m$.

We assume that the configuration space \mathcal{Q} does not contain points where the map \mathcal{H} becomes singular, i.e. its push-forward has constant rank. A singularity-free manifold $\bar{\mathcal{Q}}$ can be constructed by removing the singular points from \mathcal{Q} . Note that $\bar{\mathcal{Q}}$ is still a (now open) manifold when removing singular configurations. In order to avoid clutter, we will use the symbol \mathcal{Q} to denote the singularity-free manifold throughout the paper.

2.1 Push-Forwards and Pullbacks

Velocities are defined in the tangent spaces $\mathcal{T}_q \mathcal{Q}$ and $\mathcal{T}_x \mathcal{M}$ of the manifolds. Generalized forces being covectors lie within the dual cotangent spaces $\mathcal{T}_q^* \mathcal{Q}$ and $\mathcal{T}_x^* \mathcal{M}$, respectively. The push-forward \mathcal{H}_* associated with \mathcal{H} maps vectors in $\mathcal{T}_q \mathcal{Q}$ to vectors in $\mathcal{T}_{\mathcal{H}(q)} \mathcal{M}$ providing a local linear approximation of \mathcal{H} (Fig. 3). Similarly, the pullback \mathcal{H}^* maps covectors in $\mathcal{T}_{\mathcal{H}(q)}^* \mathcal{M}$ back to covectors in $\mathcal{T}_q^* \mathcal{Q}$. Written in coordinates, the push-forward \mathcal{H}_* will be simply the Jacobian $\mathbf{J} = \frac{\partial \mathbf{h}(\mathbf{q})}{\partial \mathbf{q}}$ and the pullback the transposed Jacobian. This vocabulary is beneficial in order to apply statements and theorems from the differential geometry world to robotics.

2.2 Forward Kinematics are Submersions

From a differential geometric perspective, the forward kinematics map of a redundant robot is a *submersion*, a map whose push-forward is surjective everywhere [Lee12], i.e., the push-forward spans the entire tangent space $\mathcal{T}_{\mathcal{H}(q)} \mathcal{M}$ for every $\mathbf{q} \in \mathcal{Q}$. Note that this requires the absence of singularities as assumed in this paper. From the submersion level set theorem [Lee12, Cor. 5.13] we know that for each $\mathbf{x}_0 \in \mathcal{M}$ the level set $\mathcal{H}(\mathbf{q}) = \mathbf{x}_0$ of \mathcal{H} is a closed embedded submanifold $\mathcal{S}_0 \subset \mathcal{Q}$, i.e., $\forall \mathbf{q} \in \mathcal{S}_0 : \mathcal{H}(\mathbf{q}) = \mathbf{x}_0$. Further, the dimension of \mathcal{S} is $n - m$. These level set submanifolds are nothing but the well-known self-motion manifolds [Bur89, MSZ94].

Taking the entirety of the level-set submanifolds of \mathcal{Q} corresponding to \mathcal{H} , a foliation of codimension $m = \dim \mathcal{M}$ is obtained. In the following we denote the dimension of the foliation by $r = n - m$. Each leaf of the foliation corresponds

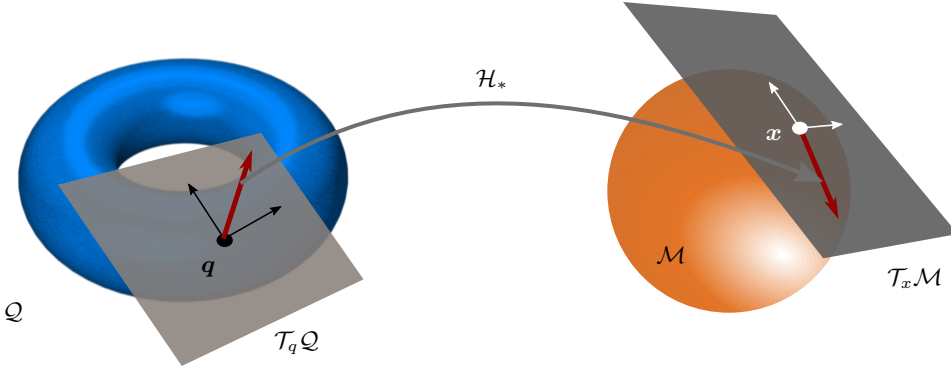


Figure 3: The push-forward transforms vectors in the tangent space $\mathcal{T}_q \mathcal{Q}$ of the configuration space to vectors in the tangent space of the task space manifold $\mathcal{T}_{\mathcal{H}(q)} \mathcal{M}$.

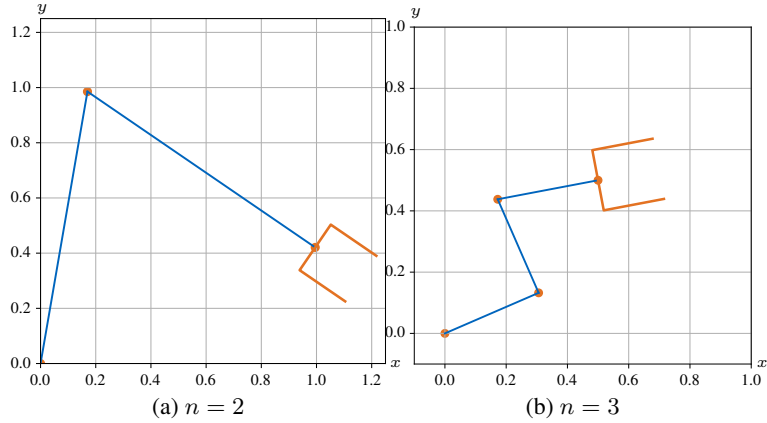


Figure 4: Planar robots with $n = 2$ and $n = 3$ degrees of freedom used as example in this paper.

to a self-motion manifold for one task configuration. In consequence, a choice of forward kinematics mapping \mathcal{H} can also be interpreted as inducing a foliation of the configuration space \mathcal{Q} . This foliation-view on forward kinematics provides insight into the global behavior of the self-motion manifolds: there is some structure present. *The self-motion manifolds fit together locally like slices in a flat chart* [Lee12, p. 501].

Consider the two degrees of freedom (DoF) example robot in Fig. 4a, whose configuration manifold is the 2-torus \mathbb{T}^2 (cf. Fig. 2). In order to obtain a kinematically redundant system, a one-dimensional task manifold and thus a scalar forward kinematics function is required. Without loss of generality, let $h(\mathbf{q}) = x$ be the chosen forward kinematics map, i.e., we only care about the x -component of the end-effector position (horizontal). The blue lines in Fig. 5a show some level sets of the forward kinematics function h . Note that the manifolds are closed on the torus \mathbb{T}^2 (Fig. 5b). Except at the singularities $\mathbf{q}_1 = [0, 0]$, $\mathbf{q}_2 = [\pm\pi, 0]$, $\mathbf{q}_3 = [0, \pm\pi]$ and $\mathbf{q}_4 = [\pm\pi, \pm\pi]$ the self-motion manifolds clearly look locally like slices of a flat chart. Also, note that those nine singular configurations in coordinate representation correspond to only four points on the torus.

The task space manifold of the above example is one-dimensional. Consequently, the codimension of the level set submanifolds is one. This corresponds to one-dimensional line-shaped self-motion manifolds.

Similarly, consider the second example robot with 3 DoF in Fig. 4b. We again consider only the x -component of the end-effector position as task space coordinate and in consequence obtain submanifolds of dimension two. Take, for instance, the submanifold of \mathcal{Q} corresponding to $h(\mathbf{q}) = 0$ shown in Fig. 6a. Now, we obtain a curved surface as self-motion manifold. Note that the surface is still closed on the 3-torus \mathbb{T}^3 . The figure shows only one leaf of the foliation. An additional rendering of multiple leaves for different level sets of $h(\mathbf{q})$ is shown in Fig. 6b. Imagine taking all of them. Then, the manifolds look locally like a stack of paper.

Finally, let us also consider the case when we define the planar Cartesian position of the end-effector as task of the 3 DoF robot (Fig. 4b), and accordingly x and y as task coordinates. Then, we obtain line-shaped self-motion manifolds as shown in Fig. 7. Note that the manifolds can be classified into two categories. One class of lines encircle the

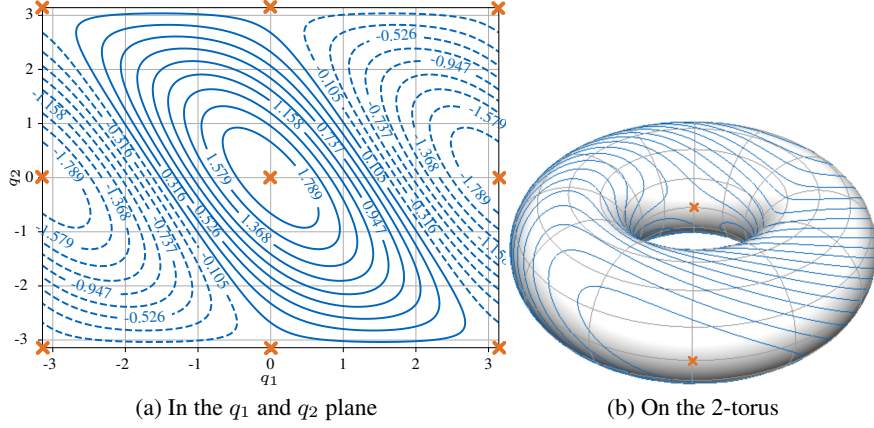


Figure 5: Foliation on the 2-torus induced by a forward kinematics function. The leaves of the foliation correspond to the well-known self-motion manifolds. In the left image, the opposing sides of the rectangle are identified to each other, according to the torus topology. The orange crosses mark the singular configurations.

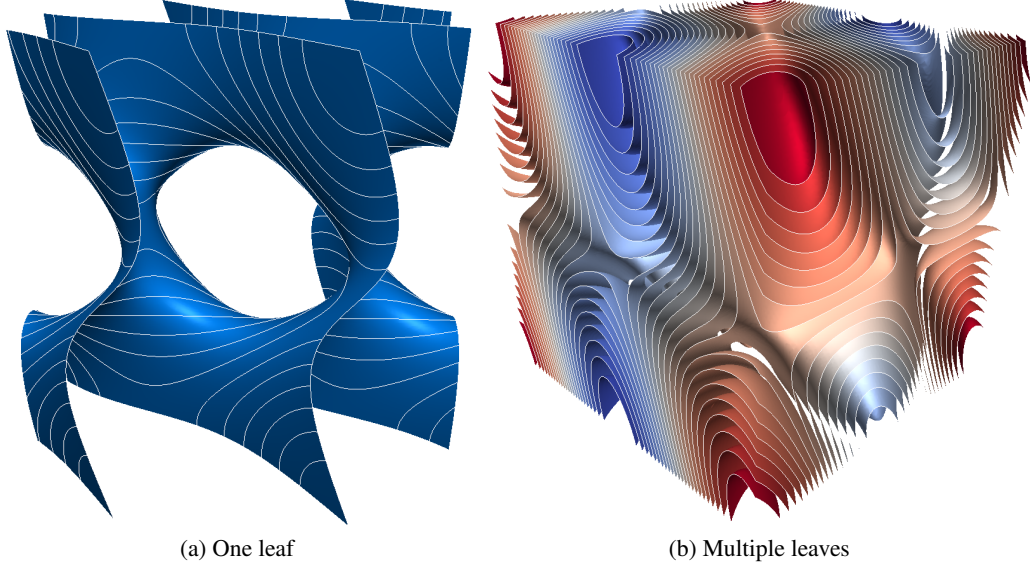


Figure 6: Self-motion manifold(s) for a planar manipulator with three degrees of freedom and the x -component of the end-effector position as single task space coordinate. The surfaces are generated using marching cubes [LLVT03] on the forward kinematics function. Note that the bounding planes of the cube are $q_i = \pi \pm \pi$ for $i \in \{1, 2, 3\}$. The boundaries disappear when embedding the manifold in the 3-torus \mathbb{T}^3 . On the left: a single leaf of the foliation. For a more intuitive visualization, you may want to 3D-print a model of this manifold. The model is provided in the supplementary material. The white lines additionally show level sets of the y -coordinate. On the right: multiple leaves of the foliation.

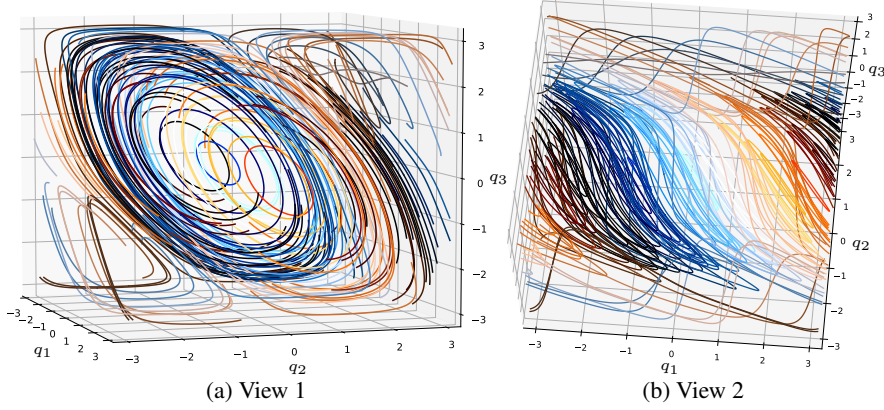


Figure 7: Foliation of codimension two of the 3-torus. Opposing faces of the cube are identified to each other. The foliation is induced by considering the planar Cartesian position of a 3-dof planar robot as task.

$q_2 = q_3 = 0$ line, while the others do not. Consider [Bur89] for a more rigorous analysis. The main observation required for this paper is that the lines form a foliation of \mathcal{Q} . Each point $q \in \mathcal{Q}$ is part of exactly one of the curves.

3 Orthogonal Foliations

The goal of this paper is to find foliations that are to the best extent possible orthogonal to the task-induced foliation $h(q)$. We will denote the constraints inducing these foliations by $\xi(q)$. $\xi(q)$ will also provide coordinates for the self-motion manifolds, which are consistent over the task foliation. Orthogonality is defined in the following sense: Given the Jacobians J_x and J_ξ defined by

$$\dot{x} = J_x(q)\dot{q} \quad (4a)$$

$$\dot{\xi} = J_\xi(q)\dot{q}, \quad (4b)$$

one would like to find $\xi(q)$ such that the two Jacobians are orthogonal with respect to the metric tensor A , i.e.

$$J_x(q)A^{-1}J_\xi^\top(q) = 0, \quad (5)$$

with $A = I$ or $A = M(q)$ depending if kinematic or dynamic decoupling is desired¹.

The property (5) corresponds to the condition on the Jacobians and projectors for the classical, velocity and torque based redundancy resolution. However, instead of first defining a null space base matrix J_ξ and checking for integrability, we follow another procedure. We start with a parametrizable foliation and then ask for orthogonality of the Jacobians. If orthogonality can be achieved everywhere, we will call the foliations *orthogonal foliations*. On the other hand, if (5) cannot be attended exactly, we will minimize the residuum over the entire considered configuration space. In the latter case, we will call the foliations *quasi-orthogonal foliations*.

3.1 Geometric Intuition of Orthogonal Foliations

Before introducing a rigorous differential geometric formulation of the proposed approach, we first explain the main ideas on some simple 2 DoF and 3 DoF examples and use and intuitive description.

Let us consider again the 3 DoF robot with 1 DoF task space (cf. Fig. 6). Fig. 1 sketches two leaves of the foliation induced by the forward kinematics, each being a manifold of dimension two. On a base leaf, say \mathcal{S}_0 defined by $h(q) = x_0$, we choose a chart ξ_{x_0} with coordinates $\{\xi_1, \xi_2\}$. The Jacobian² $J_\xi^{x_0}$ associated to ξ_{x_0} forms a basis for the tangent space at each point and thus a basis for the tangent bundle of \mathcal{S}_0 , as denoted by the red and yellow arrows. The vectors corresponding to the Jacobian J_x of the task coordinate are displayed in dark blue. Regarding the manifolds as embedded in Euclidean space, J_x is at each point orthogonal to the manifold and thus normal to the tangent space, satisfying $J_x J_\xi^\top = 0$. Now, integrating along the Jacobian J_x starting from a point $\xi_{x_0} = \{0, 0\}$ from \mathcal{S}_0 , one obtains

¹See Sec. 3.2 for clarifying why the inverse of A appears in (5).

²The superscript in $J_\xi^{x_0}$ shall denote that this Jacobian is only valid at configurations q where $h(q) = x_0$.

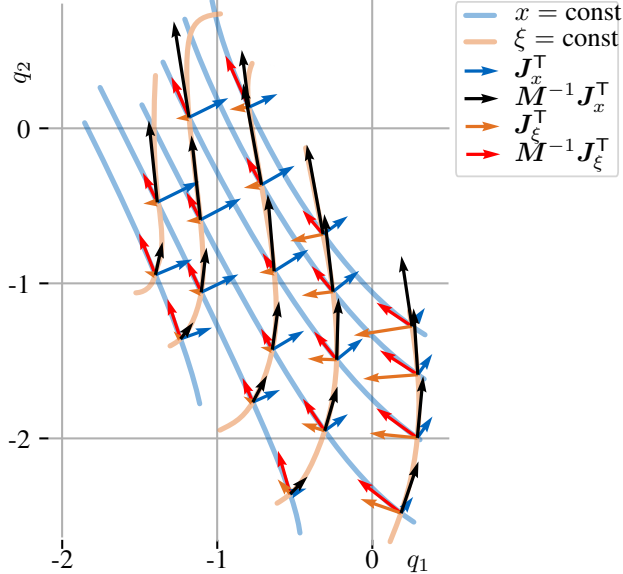


Figure 8: Orthogonal foliations for the example of a bi-dimensional configuration space and a single task coordinate for dynamic consistency.

a curve which intersects \mathcal{S}_1 . We assign the coordinates $\xi_{x_1} = \{0, 0\}$ to this point. Using this procedure, we can define locally an equivalence relation between all points in the chart ξ_{x_0} and points from \mathcal{S}_1 , thus inducing a chart ξ_{x_1} on \mathcal{S}_1 . This way, we constructed two new foliations ξ_1 and ξ_2 which are orthogonal to x in the Euclidean sense. In Fig. 1, the leaves $\xi_1 = 0$ (red) and $\xi_2 = 0$ (yellow) are exemplarily displayed. Note that the procedure described above works for any joint space dimension n , as long as the task space is one-dimensional and thus the dimension of the task-space induced foliation is $n - 1$.

The above example leads to foliations ξ satisfying the generalized orthogonality condition (5) for $\mathbf{A} = \mathbf{I}$. For the case $\mathbf{A} = \mathbf{M}(\mathbf{q})$ the geometric interpretation and visualization gets more complex and will be therefore discussed for the 2 DoF case with 1 DoF task space presented before. The task-induced foliation is thus one-dimensional. Some of its leaves \mathcal{S}_i are displayed as blue curves in Fig. 8. In dark blue, the Jacobian \mathbf{J}_x is displayed. As usual, it satisfies $\mathbf{J}_x(\mathbf{q})\mathbf{v} = 0$ for any tangent vector $\mathbf{v} \in \mathcal{T}_q \mathcal{S}_i$ ³. The condition $\mathbf{J}_x \mathbf{M}^{-1} \mathbf{J}_\xi^T = 0$ thus implies that $\mathbf{M}^{-1} \mathbf{J}_\xi^T$ is now tangent to the foliation and thus forms a basis for the null space of \mathbf{J}_x . This vector field is displayed by red arrows in Fig. 8. It is therefore obvious that in this case \mathbf{J}_ξ , which is orthogonal to the ξ foliation, does not belong to the tangent bundle of the task foliation, but is rotated accordingly, as shown by the orange arrows. Finally, note that the leaves of the ξ foliation are obtained by integrating the $\mathbf{M}^{-1} \mathbf{J}_x^T$ vector field, displayed in black.

As a conclusion, the orthogonal foliation for dynamic consistency has $\mathbf{M}^{-1} \mathbf{J}_x^T$ as tangent vectors and \mathbf{J}_ξ as normal vectors, while the task foliation has $\mathbf{M}^{-1} \mathbf{J}_\xi^T$ as tangent vector and \mathbf{J}_x as normal vector. Again, these results can be easily extended to configuration spaces of any dimension as long as the task space has 1 DoF only.

Finally, let us consider the 3 DoF case, with 2 DoF task space. For simplicity, the Euclidean orthogonality condition is considered again, i.e. $\mathbf{A} = \mathbf{I}$. The task foliation consists of curves, as displayed in Fig. 9. The rows of the Jacobian \mathbf{J}_x span now a plane that is orthogonal to the corresponding task foliation leaf at each point. They define two vector fields in the tangent bundle. For these vector fields to be integrable, they need to satisfy the Frobenius theorem [Fro77]. In general this condition will, however, not be satisfied.

Take a configuration \mathbf{q}_0 . This will be part of exactly one leaf, i.e., $\mathbf{q}_0 \in \mathcal{S}_0$ of the task foliation, which corresponds to the task configuration \mathbf{x}_0 . Now, we follow the vector fields given by the rows of the Jacobians as shown in Fig. 9. We take two different paths leading to the same task configuration $\mathbf{h}(\mathbf{q}_a) = \mathbf{h}(\mathbf{q}_b) = \mathbf{x}_1$. Due to the non-involutivity we will generally have $\mathbf{q}_a \neq \mathbf{q}_b$, where $\mathbf{q}_a, \mathbf{q}_b \in \mathcal{S}_1$. Therefore, the two final configurations \mathbf{q}_a and \mathbf{q}_b cannot form, together with \mathbf{q}_0 , a single leaf of an orthogonal foliation. When following the flow of the gradients from one task foliation to another, the final configuration will depend on the path taken to reach it, which is the essence of non-integrability. In the infinitesimal case, the difference $\mathbf{q}_b - \mathbf{q}_a$ corresponds to the Lie bracket $[\mathbf{J}_{x_1}^T, \mathbf{J}_{x_2}^T]$ of the two vector fields. In

³By $\mathcal{T}_q \mathcal{S}$ we refer to the subspace $\mathcal{T}_q \mathcal{S} \subset \mathcal{T}_q \mathcal{Q}$ of the tangent space $\mathcal{T}_q \mathcal{Q}$ spanned by the tangent vectors of the embedded submanifold $\mathcal{S} \subset \mathcal{Q}$, i.e. the tangent vectors of $\mathcal{T}_{\xi(\mathbf{q})} \mathcal{S}$ given as embedded vectors in $\mathcal{T}_q \mathcal{Q}$.

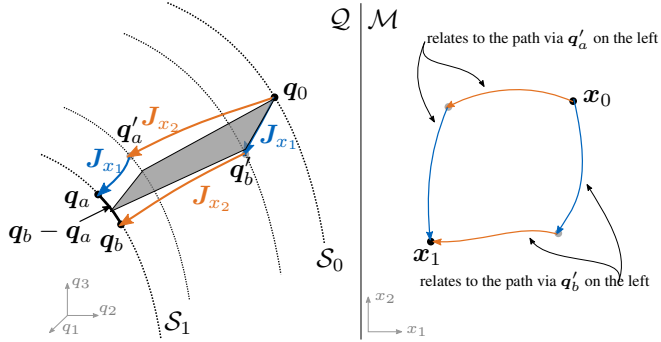


Figure 9: The distribution of vector fields spanned by the task space Jacobian is generally non-involutive.

general, there is no integral surface which, even locally, is orthogonal to every leaf of the task foliation and which would intersect \mathcal{S}_1 in a single point independent of the path.

However, in this case, one can pose the question of finding the surface, which is *as orthogonal as possible* to the task foliation, where the optimization is formulated in a least mean square sense. This means, in our case, that the Jacobian \mathbf{J}_x is *as tangent as possible* to the desired foliation ξ . A leaf of this foliation, passing through q_0 is visualized in gray in Fig. 9.

3.2 Null Space Jacobians and Projectors

Let us return to the relation between null space basis $\mathbf{J}_\xi(\mathbf{q})$ and projection matrix $\mathbf{P}(\mathbf{q})$, as mentioned in the introduction. Independent of the existence question about an integral manifold, a null-space basis on velocity level, as defined in (4a)-(5), can always be constructed. In compact form, (4a)-(4b) can be written as

$$\dot{\varphi} = \mathbf{J}(\mathbf{q})\dot{\mathbf{q}}, \quad (6)$$

with $\dot{\varphi} = [\dot{\mathbf{x}}^\top \quad \dot{\xi}^\top]^\top$ and

$$\mathbf{J}(\mathbf{q}) = \begin{bmatrix} \mathbf{J}_x(\mathbf{q}) \\ \mathbf{J}_\xi(\mathbf{q}) \end{bmatrix}. \quad (7)$$

Since $\dot{\xi}$ has been constructed such that $\mathbf{J}(\mathbf{q})$ is full rank, the stacked Jacobian $\mathbf{J}(\mathbf{q})$ can be inverted. It can be easily verified using (5) that the inverse is

$$\mathbf{J}^{-1}(\mathbf{q}) = \begin{bmatrix} \mathbf{J}_x^{\#A}(\mathbf{q}) & \mathbf{J}_\xi^{\#A}(\mathbf{q}) \end{bmatrix}, \quad (8)$$

since $\mathbf{J}(\mathbf{q})\mathbf{J}^{-1}(\mathbf{q}) = \mathbf{I}$. This, of course, implies as well $\mathbf{J}^{-1}(\mathbf{q})\mathbf{J}(\mathbf{q}) = \mathbf{I}$, which leads to

$$\mathbf{J}_x^{\#A}(\mathbf{q})\mathbf{J}_x(\mathbf{q}) + \mathbf{J}_\xi^{\#A}(\mathbf{q})\mathbf{J}_\xi(\mathbf{q}) = \mathbf{I}. \quad (9)$$

Therefore, a simple relation exists between the projector $\mathbf{P}(\mathbf{q})$ defined as in (2), using the task Jacobian, and the null space basis $\mathbf{J}_\xi(\mathbf{q})$, namely

$$\mathbf{P}(\mathbf{q}) = \mathbf{I} - \mathbf{J}_x^{\#A}(\mathbf{q})\mathbf{J}_x(\mathbf{q}) = \mathbf{J}_\xi^{\#A}(\mathbf{q})\mathbf{J}_\xi(\mathbf{q}). \quad (10)$$

This makes clear that in cases in which exact orthogonality as demanded in (5) can be achieved for the foliation $\xi(\mathbf{q})$, projection based control approaches are equivalent on velocity and torque level to the controllers based on the orthogonal manifold, while the latter has the advantage of additionally providing a coordinate (position) level. If the manifold orthogonality is only approximate, an additional projection can be performed, while the projection only has to remove the residual error in this case.

3.3 On Coordinate Independence

In the next section, we will formulate the approach using language from differential geometry, which provides a coordinate invariant perspective. Before that, we aim at briefly clarifying why the integrability conditions on \mathbf{J}_x are indeed coordinate-independent, by looking at a concrete example. Take the 3 DoF manipulator with two-dimensional task space and consider two different choices of task coordinates

$$\begin{bmatrix} x \\ y \end{bmatrix} = \mathbf{h}_c(\mathbf{q}) \text{ and } \begin{bmatrix} r \\ \varphi \end{bmatrix} = \mathbf{h}_p(\mathbf{q}), \quad (11)$$

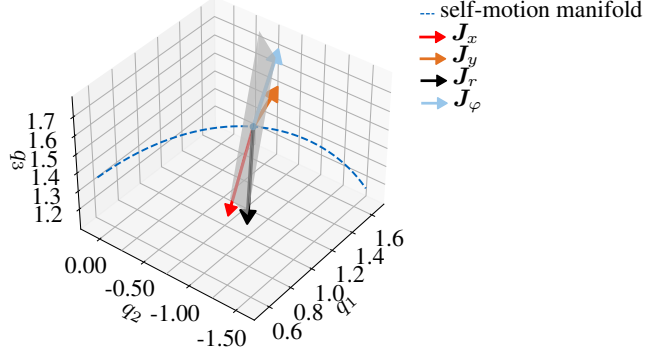


Figure 10: The subspace spanned by the rows of the task Jacobian does not depend on the choice of task coordinates. The task is the position of the end-effector. We evaluate the Jacobian and plot the rows for Cartesian coordinates (red and orange) and for polar coordinates (black and light-blue). The gray plane visualizes the 2d subspace spanned by all four vectors.

where both specify the position of the end-effector, once in Cartesian and once in polar coordinates. In the latter case, r represents the radius and φ the angle. The associated $(\mathbb{R}^{2 \times 3})$ Jacobians are

$$\begin{bmatrix} \dot{x} \\ \dot{y} \end{bmatrix} = \mathbf{J}_c(\mathbf{q})\dot{\mathbf{q}} \text{ and } \begin{bmatrix} \dot{r} \\ \dot{\varphi} \end{bmatrix} = \mathbf{J}_p(\mathbf{q})\dot{\mathbf{q}}, \quad (12)$$

where $\mathbf{J}_c = \partial \mathbf{h}_c / \partial \mathbf{q}$ and $\mathbf{J}_p = \partial \mathbf{h}_p / \partial \mathbf{q}$.

Next, consider the function $\text{pol}(x, y) = (r, \varphi)$ mapping positions in the plane from Cartesian to polar coordinates. One can write the function \mathbf{h}_p as a composition of \mathbf{h}_c and pol , i.e.,

$$\mathbf{h}_p(\mathbf{q}) = \text{pol}(\mathbf{h}_c(\mathbf{q})). \quad (13)$$

Let $\mathbf{J}_{\text{pol}} \in \mathbb{R}^{2 \times 2}$ denote the Jacobian of pol and let us differentiate (13)

$$\begin{bmatrix} \dot{r} \\ \dot{\varphi} \end{bmatrix} = \mathbf{J}_{\text{pol}} \mathbf{J}_c \dot{\mathbf{q}} = \mathbf{J}_p \dot{\mathbf{q}}. \quad (14)$$

It follows that $\mathbf{J}_p = \mathbf{J}_{\text{pol}} \mathbf{J}_c$. If \mathbf{J}_{pol} is full-rank, then \mathbf{J}_p and \mathbf{J}_c will have the same null space. Moreover, the rows of \mathbf{J}_c and \mathbf{J}_p all span the same subspace of \mathbb{R}^3 , which is orthogonal to the self-motion manifold at each point. Fig. 10 shows this for one point on one of the task foliations.

This reasoning is valid for any dimension of configuration and task space. In differential geometric terms, the orthogonal linear subspaces at all points of the task foliation form a distribution whose integrability we are interested in. This distribution only depends on the task manifold, but not on its specific coordinates. Different choices of coordinates on the task manifold will create different vector fields. These, however, will all span the same distribution.

3.4 Differential Geometric Formulation

The dynamics of a multi-body system can be naturally associated to a Riemannian manifold (\mathcal{Q}, g) [SW15, DCGP19], i.e., we equip the configuration manifold with a Riemannian metric g . For mechanical systems, a natural choice for the metric is the inertia tensor of the system. Hence, the metric g is simply the coordinate-invariant version of the mass matrix $\mathbf{M}(\mathbf{q})$. In this section, we use the symbols g_I and g_M to denote the coordinate-invariant versions of the metrics, which in coordinates are represented by \mathbf{I} and $\mathbf{M}(\mathbf{q})$, respectively. Likewise, the metric g_A denotes a metric that can be any Riemannian metric including g_I and g_M ⁴.

In the previous sections, we considered the configuration space being Euclidean, identifying the covectors with their vector counterparts (w.r.t. the Euclidean metric) and visualizing them accordingly. While this is not very elegant from a differential geometric perspective, we think that the section provides useful and comprehensive insights for roboticists.

From the differential geometric perspective, the rows of the Jacobian, being derivatives of scalar functions, are coordinate versions of differential one-forms (or covectors). Consider a task space parametrized by a set of task coordinates $\mathbf{x} \in \mathcal{M}$

⁴This choices of using the Euclidean and the inertia tensor as metric are not complete. Arbitrary custom metrics can be used here, e.g., the stiffness matrix for stiffness consistence [DOAS15].

and a forward kinematics $\mathbf{x} = \mathbf{h}(\mathbf{q})$. The differential one-form associated to each coordinate x_i is (e.g. [PK98])

$$dh_i = \sum_{j=1}^n \frac{\partial h_i(\mathbf{q})}{\partial q_j} dq_j = \mathbf{J}_{x_i} d\mathbf{q}, \quad (15)$$

the elements of the one-form thus being the corresponding row of the Jacobian. Taking a self-motion manifold \mathcal{S}_0 defined by $\mathbf{h}(\mathbf{q}) = \mathbf{x}_0$ for an arbitrary constant \mathbf{x}_0 , and considering a velocity $\mathbf{v} \in \mathcal{T}_q \mathcal{S}_0$, the reciprocal relation $dh_i(\mathbf{v}) = 0$ holds. Applying a one-form to a vector is independent of any metric.

Moreover, having defined a metric g_A on \mathcal{Q} associates a vector to any covector in a natural way. In particular, the gradient $\nabla_A h_i$ is the vector associated to the one-form dh_i . The gradient $\nabla_A h_i$ does not only depend on the function itself, but also on the metric. In coordinates, the gradient $\nabla_A h_i$ is obtained by multiplying the partial derivatives by the inverse metric tensor, an operation known as *raising an index* in tensor calculus⁵

$$\nabla_A h_i = \mathbf{A}^{-1} \begin{bmatrix} \frac{\partial h_i(\mathbf{q})}{\partial q_1} \\ \vdots \\ \frac{\partial h_i(\mathbf{q})}{\partial q_m} \end{bmatrix} = \mathbf{A}^{-1} \mathbf{J}_{x_i}^\top. \quad (16)$$

As an inverse operation, one associates a covector to a vector by *lowering an index*. In our case this is $\mathbf{J}_{x_i}^\top = \mathbf{A} \nabla_A h_i$.

Therefore, (5) can be interpreted as applying one-forms to gradients. We take the one-forms dh_i for $i \in \{1..m\}$, and apply them to the gradients $\nabla_A \xi_j$ for $j \in \{1..r\}$ and require them to vanish

$$dh_i(\nabla_A \xi_j) = 0. \quad (17)$$

Due to the symmetry of the metric, the roles in (17) can be swapped

$$d\xi_j(\nabla_A h_i) = 0. \quad (18)$$

Note that, again, the metric does not appear explicitly here, but is, of course, contained in the definition of the gradient. However, the same condition can be expressed in form of vector orthogonality as $\nabla_A^\top h_i \mathbf{A} \nabla_A \xi_i = 0$ or in form of covector orthogonality as $dh_i \mathbf{A}^{-1} d\xi_i^\top = 0$. This should clarify why we talk about orthogonality w.r.t. the metric \mathbf{A} in (5), although its inverse appears in the formula. From this perspective, it becomes clear that in Sec. 3.1 and Fig. 1, Fig. 8, and Fig. 9 we actually visualize gradients w.r.t. either the metric \mathbf{I} or $\mathbf{M}(\mathbf{q})$.

Gradients and one-forms can be defined in a coordinate-independent way. Therefore, (18) can be thought of as coordinate-free version of our main condition (5).

In order to conclude under which conditions functions ξ_j satisfying (18) exist, we need to introduce the notion of an exterior differential system (EDS) [McK20, BGG03, BCG⁺91]. An EDS is a tuple $(\mathcal{Q}, \mathcal{I})$ of a manifold and an ideal of k-forms. Integral elements of the EDS are linear subspaces of the tangent space of \mathcal{Q} on which forms in \mathcal{I} vanish [McK20].

Condition (18) can be reinterpreted using EDS-language: find an EDS $(\mathcal{Q}, \mathcal{I})$ such that the one-forms $d\xi_j$ in \mathcal{I} are the differentials of functions ξ_j and such that the integral elements are spanned by $\nabla_A h_i$. This is opposite to classical EDS problems, where the ideal of k-forms \mathcal{I} is given and the integral elements are unknowns.

Let Δ_h denote a distribution [Lee12, Ch. 19] of vector fields, which is locally spanned by

$$\Delta_h = \text{span}\{\nabla_{g_A} h_1, \dots, \nabla_{g_A} h_m\}. \quad (19)$$

The distribution Δ_h will generally not be involutive [KH83].

From the Frobenius theorem for EDSs [McK20, Thm. 1.3] we know that the integral manifolds of \mathcal{I} form the leaves of a foliation of \mathcal{Q} iff the vector fields on which all forms in \mathcal{I} vanish are closed under the Lie bracket and thus involutive. This is in general not the case for our redundancy resolution problem, as the distribution Δ_h is generally not involutive. However, it will be trivially involutive, if one has a one-dimensional task space and a single task coordinate, as a one-dimensional distribution is always involutive. These statements can be formalized as follows.

Theorem 1 (Existence of Orthogonal Foliations) *A task induced foliation admits orthogonal foliations if and only if the distribution formed by the gradients of the task coordinates is involutive.*

Corollary 1 *A one-dimensional task space always admits orthogonal foliations.*

⁵In (15) and (16) we stick to the convention of representing contravariant vectors as columns and covectors as rows.

Note that the above statements are coordinate invariant and depend only on the forward kinematics map. Indeed, taking different coordinate charts on the task manifolds leads to different gradients, but they all span the same space.

Take, for instance, a three-dimensional configuration space and a single task coordinate. Two orthogonal foliations ξ_1 and ξ_2 need to be determined in this case. This kind of problem has been studied in some publications, where it is known as *triply orthogonal system* [BMS03, SG08] or *triply orthogonal web* [McK20]. These publications, however, ask that the foliations ξ_1 and ξ_2 are orthogonal as well. This is a condition which we relax in this work, as one usually cannot expect it to be satisfied.

Theorem 1 provides a necessary and sufficient condition for the task induced foliation to admit orthogonal foliations. Throughout the paper, we will deal with two cases satisfying the condition and one that does not. In the latter case, we show that we can find an approximate solution by relaxing the conditions and optimizing a cost function.

4 Local Solution: Plane Stacks

Before beginning with a more rigorous study on how to generate orthogonal foliations $\xi(\mathbf{q})$, we start with a simple base-line version, where linear, locally orthogonal foliations are used. In particular, we will approximate each orthogonal coordinate $\xi_j(\mathbf{q})$ by a function, which is linear in \mathbf{q} .

Therefore, we construct a foliation where the leaves are planes. Consider a configuration $\mathbf{q}_0 \in \mathcal{Q}$, which we call the *base configuration for the locally orthogonal foliations* and also consider a hyperplane $E_0 = E(\mathbf{q}_0, \mathbf{n}_0)$ with support vector \mathbf{q}_0 and unit normal vector \mathbf{n}_0 . The signed distance of a query point \mathbf{q} to the hyperplane can be computed using the Hesse normal form of the plane

$$d(E_0, \mathbf{q}) = \mathbf{n}_0^\top (\mathbf{q} - \mathbf{q}_0) \quad (20)$$

In fact, this signed distance function can also be interpreted as a coordinate function with a trivial Jacobian being the covector version of \mathbf{n}_0 .

Equation (20) also creates a foliation for which each leaf $E_n = E(\mathbf{q}_n, \mathbf{n}_0)$ is a hyperplane of constant distance and thus parallel to the base hyperplane E_0 . Locally, around \mathbf{q}_0 , the function $\xi_j(\mathbf{q}) = d(E_0, \mathbf{q})$ provides approximate orthogonal coordinates if the normal vector \mathbf{n}_0 is chosen appropriately. For each locally orthogonal foliation $\xi_j(\mathbf{q})$ we require a unit normal vector \mathbf{n}_j such that they are mutually linearly independent. Additionally, we require the normal vectors \mathbf{n}_j to span the orthogonal complement of the rows of $\mathbf{J}_x(\mathbf{q}_0)$ for Euclidean metric or of the columns of $\mathbf{M}^{-1}(\mathbf{q}_0) \mathbf{J}_x^\top(\mathbf{q}_0)$ for inertia metric, respectively. In other words, we can say that the unit vectors associated to the functions $\xi_j(\mathbf{q})$ span the null space of $\mathbf{A}^{-1}(\mathbf{q}_0) \mathbf{J}_x(\mathbf{q}_0)$.

The entirety of locally orthogonal coordinates can be written in compact form

$$\xi(\mathbf{q}) = \underbrace{\begin{bmatrix} \mathbf{n}_1^\top \\ \vdots \\ \mathbf{n}_r^\top \end{bmatrix}}_{\mathbf{J}_\xi} (\mathbf{q} - \mathbf{q}_0). \quad (21)$$

Note that the Jacobian \mathbf{J}_ξ of $\xi(\mathbf{q})$ is constant. Based on this construction we ensure that (5) is satisfied at \mathbf{q}_0 . Consequently, at \mathbf{q}_0 , the orthogonal coordinates $\xi(\mathbf{q})$ are dynamically decoupled from the task. The performance on the regions around \mathbf{q}_0 will depend on the curvature of the self-motion manifolds and the behavior of the metric. For configurations that are far from the base configuration for the locally orthogonal foliations, the function (21) cannot be expected to perform well.

5 Numerical Coordinate Growing

In this section, we show how an orthogonal foliation can be numerically generated for the case of a one-dimensional task space. In order to perform the numerical propagation of the orthogonal foliation coordinates, we start by selecting one value for the task-coordinate function and call it x_0 . Then, we compute the corresponding self-motion manifold \mathcal{S}_0 such that

$$\forall \mathbf{q} \in \mathcal{S}_0 : \mathbf{h}(\mathbf{q}) = \mathbf{x}_0. \quad (22)$$

We call \mathcal{S}_0 the *base manifold* in the following. Note that $\dim \mathcal{S}_0 = n - 1$. Then, we define a chart $\xi_0 : \mathcal{S}_0 \rightarrow \mathbb{R}^{n-1}$ on the base manifold.

We determine the coordinates $\xi(\mathbf{q}_1)$ of a point $\mathbf{q}_1 \in \mathcal{S}_1$ on another leaf \mathcal{S}_1 by taking the differential equation

$$\dot{\mathbf{q}} = (\mathbf{x}_0 - \mathbf{h}(\mathbf{q})) \nabla_{\mathbf{A}} \mathbf{h}(\mathbf{q}) \quad (23)$$

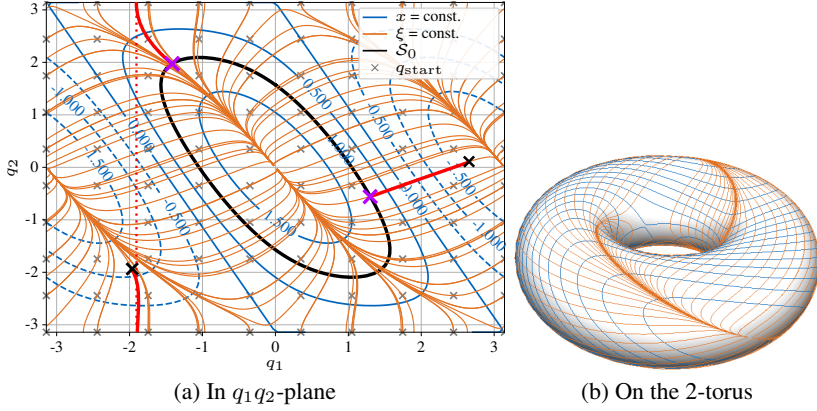


Figure 11: Following the gradient flow of the x -coordinates for Euclidean metric.

with initial condition $\mathbf{q}(0) = \mathbf{q}_1$. The flow (23) will converge onto the base manifold at a point $\hat{\mathbf{q}} \in \mathcal{S}_0$. We then set $\xi(\mathbf{q}_1) = \xi_0(\hat{\mathbf{q}})$ to obtain the coordinates of $\mathbf{q}_1 \in \mathcal{S}_1$.

In the following sections, we investigate the resulting coordinates for the two example robots for both, Euclidean and inertia tensor as Riemannian metrics. The point of convergence of the gradient flow (23) is numerically evaluated using a Runge-Kutta integration scheme [HNW08]. We stop the integration when the change of \mathbf{q} between two integrator steps falls below a threshold of 10^{-6} .

5.1 In Two-Dimensional Configuration Space

Consider the example manipulator with two degrees of freedom (Fig. 4a) and select the x -component of the end-effector position as task coordinate.

5.1.1 Euclidean Metric ($\mathbf{A} = \mathbf{I}$)

We begin with the choice $\mathbf{A} = \mathbf{I}$, i.e. we choose the standard Euclidean metric on \mathcal{Q} . Fig. 11a shows isolines of the forward kinematics function in blue.

Suppose we take a grid of points in the configuration space denoted by the gray crosses. We take the gradient flow $\pm \nabla_I h(\mathbf{q})$ and integrate it into both directions for each point of the grid. The orange lines in Fig. 11a show the resulting integral curves. Dependent on the sign, the flow converges to one of the singularities. Note the toroidal topology of the configuration space. Especially, the points of convergence on both sides of the plot are identified to the same point on the torus. While the singularities at $q_2 = 0$ are stable or unstable nodes dependent on the sign of the flow, the singularities at $q_2 = \pm\pi$ are saddles. Fig. 11b shows the lines additionally on the 2-torus. The entirety of integral curves also foliates the configuration space \mathcal{Q} .

We pick a base manifold \mathcal{S}_0 such that $x_0 = 1$, which is depicted by the black curve in Fig. 11a. The base manifold is homeomorphic to the 1-sphere \mathbb{S}^1 . Consequently, we cannot find a global diffeomorphism $\xi_0 : \mathcal{S}_0 \rightarrow \mathbb{R}$. Instead, we can find a smooth function $\hat{\xi}_0 : \mathcal{S}_0 \rightarrow \mathcal{SO}(2)$. The diffeomorphism $\hat{\xi}_0$ needs to be used if the entire base manifold \mathcal{S}_0 shall be covered. However, here we apply a simplification and map the entire manifold \mathcal{S}_0 but one point to $(-\pi, \pi]$ to stay within one coordinate chart. This comes with the drawback that ξ_0 cannot be used at $\pm\pi$ and we cannot pass through that point.

Finally, we evaluate the resulting coordinate function $\xi : \mathcal{Q} \rightarrow (-\pi, \pi]$ by pulling a point $\mathbf{q} \in \mathcal{Q}$ onto the base manifold (23) and evaluating ξ_0 at that point. This procedure is visualized for two example configurations in Fig. 11. When starting from arbitrary joint configurations (black crosses), the flow will trace out a path (red lines) and converge at a configuration on the base manifold (violet crosses). Fig. 12a shows the function color-coded.

In large regions of Fig. 12a the function looks smooth. However, there are also edges of jumps in the color rendering of ξ . At the origin $\mathbf{q} = (0, 0)^\top$ is a discontinuous jump, while it becomes continuous still being steep when following the edge outwards. The other edges can be moved to the boundary by considering the toroidal structure of the space and solving the puzzle. The small sketch in the top-right corner of Fig. 12a visualizes this idea. As we assumed the configuration space singularity-free by taking out the singular configurations, the discontinuous spot can be neglected. Within the white region of Fig. 12a is another discontinuous spot, which is an artifact of the mapping of \mathbb{S}^1 onto \mathbb{R} .

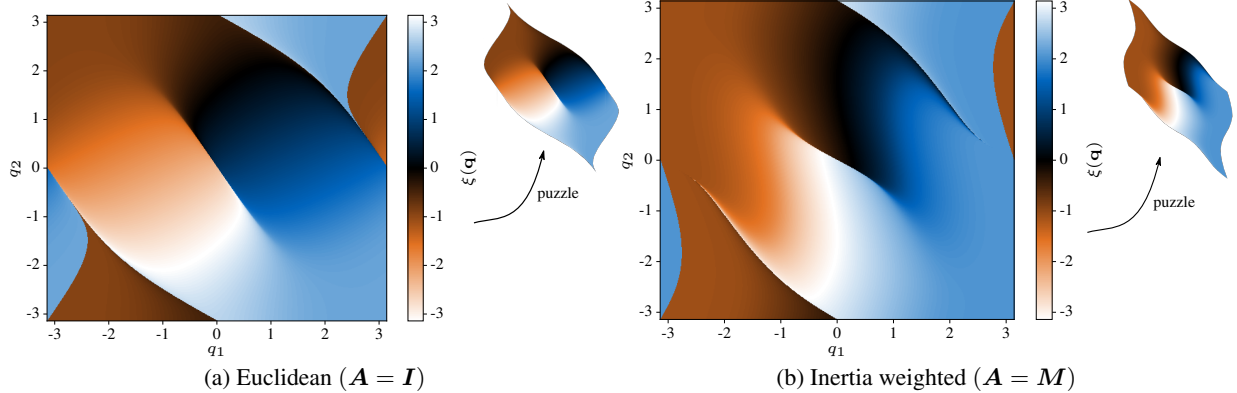


Figure 12: Orthogonal coordinate function $\xi(\mathbf{q})$ for Euclidean metric (left) and non-Euclidean metric (right). The color encodes the value of the function $\xi(\mathbf{q})$. Sketches on the top-right: most discontinuities can be pushed to the boundary when considering the toroidal structure.

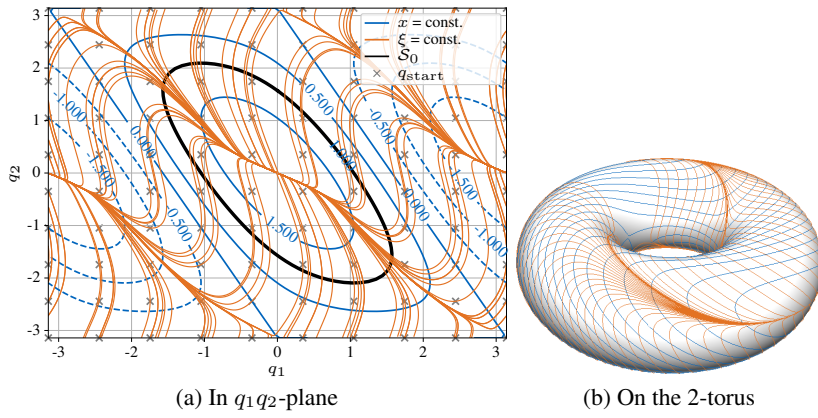


Figure 13: Following the gradient flow of the x -coordinate for inertia tensor as metric ($\mathbf{A} = \mathbf{M}$).

5.1.2 Mass Metric ($\mathbf{A} = \mathbf{M}$)

The function ξ_0 does not change compared to the previous example. On \mathcal{S}_0 we obtain the same values for ξ as before. What, however, does change are the values of points in $\mathcal{Q} \setminus \mathcal{S}_0$. In comparison to the Euclidean case, the coordinates on \mathcal{S}_0 are propagated into different directions as the gradient in (23) depends on the metric.

Fig. 13 shows integral curves of $\pm \nabla_{\mathbf{M}} h(\mathbf{q})$ (orange), as well as the contour lines of the task coordinate (blue) and the grid of start points q_0 (gray crosses) for the integration and Fig. 12b shows the coordinate function color-coded.

5.2 In Three-Dimensional Configuration Space

Next, we consider the case of $n = 3$ degrees of freedom of the manipulator and we choose the x -component of the end-effector pose as task-coordinate, i.e., the task space manifold is $m = 1$ -dimensional. Therefore, we obtain a $r = 2$ -dimensional foliation of the configuration space by the self-motion manifolds.

We again select a base manifold \mathcal{S}_0 and define a coordinate chart on it (cmp. Fig. 1). Parametrization of a surface embedded in three-dimensional space is a well-studied problem within the field of computer graphics [FH05], where this is required for, among others, texture mapping. We consider the simplest case of parametrization: a surface of disk-topology. This does not involve the need for cuts of the surface for parametrization.

Within the computer graphics field the desired object is a parametrization $\Phi : \mathcal{X} \rightarrow \mathcal{S}_0$, where $\mathcal{X} \subset \mathbb{R}^2$ is a region in the parameter space. A mapping Φ is one-to-one if

1. Φ maps the boundary $\partial \mathcal{S}_0$ of the surface to the boundary $\partial \mathcal{X}$ of a convex region $\mathcal{X} \subseteq \mathbb{R}^2$ and

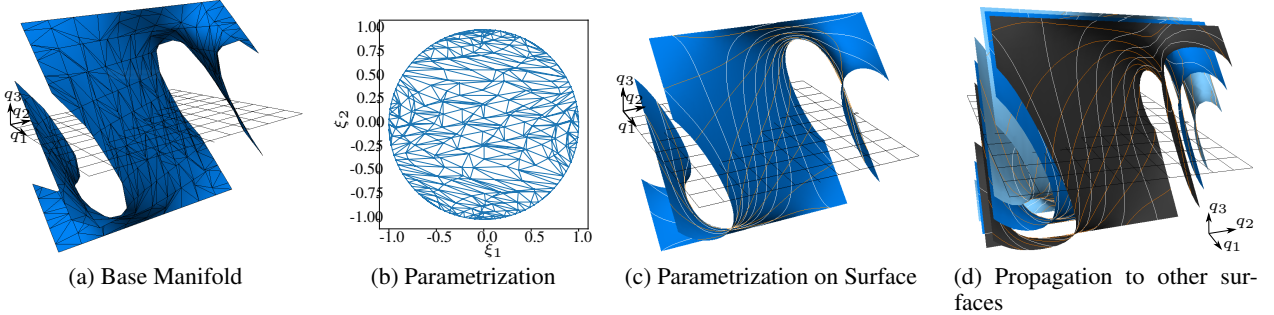


Figure 14: Coordinate growing from a base manifold S_0 . **(a)** Triangulation of the base manifold shown for a coarse resolution of the triangle mesh. **(b)** Parametrization of the base manifold onto the unit circle. The same triangulation is used as in (a). The edges do not intersect and we obtain a bijection between the unit circle and the base manifold. **(c)** Visualization of the parametrization on the base manifold using isolines of the parametrization. **(d)** Propagation to other leaves of the foliation.

2. Φ is harmonic [Rad26, Kne26, Cho45].

Within this context *harmonic* refers to the property $\Delta\Phi = 0$, i.e., the application of the Laplace-Beltrami operator to Φ vanishes everywhere [SA01]. The parametrization function Φ is the inverse of our desired chart of the base manifold $\xi_0 = \Phi^{-1}$.

We select $x_0 = 0$ and constrain $q_1 \geq 0$, i.e. we consider a subregion of the configuration space \mathcal{Q} and the simplified model generated here will only be valid in this subregion. By this constraint, we achieve a disk-topology of S_0 . Further, we apply marching cubes [LLVT03, LC87] and obtain a triangle mesh approximating the base manifold S_0 as shown in Fig. 14a. Because of the mesh structure, we can use discrete differential geometry to rewrite the continuous constraints for Φ in a discrete fashion and the condition boils down to solving a linear system of equations as summarized in Sec. 10. Boundary conditions are required for the linear system, which we generate by mapping the boundary of the base manifold to the unit circle. Afterwards, we solve for the interior vertices and obtain a discrete version of a bijective mapping between the base manifold and the unit disk in the plane (Fig. 14b). Fig. 14c additionally shows isolines of the parameter space on the base manifold. The visualizations are shown for a coarse resolution of the triangle mesh in order to visualize the mesh structure in the parametrization domain.

Following the above procedure, we obtain a discrete version of $\xi_0(q)$ by having a unique value $\xi_0(q)$ for every vertex of the mesh. For every other point $q \in S_0$, which does not coincide with a vertex of the mesh, we query a KDTree [MM99] of the mesh to find the face containing q (approximately). Afterwards, we interpolate between the values for ξ_0 of the three vertices of the face.

Then, we follow the gradient flow (23) to pull any configuration q onto the base manifold $\hat{q} \in S_0$ and interpolate $\xi_0(\hat{q})$ as stated above. We have achieved a coordinate function $\xi : \bar{\mathcal{Q}} \rightarrow \mathbb{R}^2$.

Fig. 14d shows the result for $A = I$. We show three self-motion manifolds and the isolines of the coordinate functions ξ_1 and ξ_2 . The dark blue manifold in the middle of the stack is the base manifold S at $x_0 = 0$ while the other manifolds (gray and light blue) correspond to $x = \pm 0.3$.

6 Neural Network Approximation

The previous section showed how a coordinate function defined on one of the self-motion manifolds can be propagated to other points in the configuration space for the case of only one task coordinate. However, this approach has mainly three drawbacks: (1) the algorithm is rather expensive in execution time, (2) there is no easy way to obtain a Jacobian J_ξ besides the obvious numerical Jacobian, which comes at the cost of large computational effort and (3) it only works for one-dimensional tasks. For higher dimensional task-space, there are also multiple gradient flows (23), one for each row of the Jacobian. Therefore, there are multiple directions in which the coordinates of the base manifold would need to be propagated to. For the same approach to work for higher dimensional task spaces, all the flows (23) starting from a point $q_1 \in S_1$ would need to end at the same point in $q_0 \in S_0$. This, however, is in general not possible due to non-involutivity of the gradients of the task coordinates. For the one-dimensional task we could follow the gradient

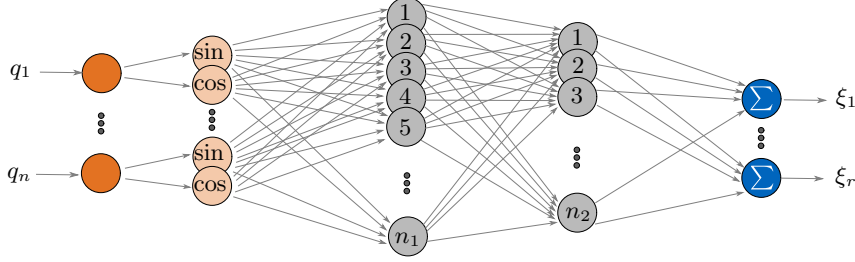


Figure 15: Neural network with two hidden layers. The outputs are the coordinate functions ξ_i . Before feeding the inputs q_i to the actual network we apply the sine and cosine of each input value in order to implement the toroidal structure of the input space.

flow and observed that the resulting curves generated a foliation of \mathcal{Q} . There exists in general no foliation such that all gradients of the task coordinates are tangent to the leaves of the foliation.

In this section we therefore relax the orthogonality condition to *as orthogonal as possible*, in a least mean square sense. If exact integrability is not given, we use a smooth parametric function $\xi_\theta(\mathbf{q})$ and optimize the parameters θ such that the resulting foliation is as tangent as possible to the gradients of the task coordinates. Another benefit of this approach is the smooth nature of the parametric function, which allows for analytical Jacobians. The function $\xi_\theta(\mathbf{q})$ can be optimized offline, and during execution one can use a fast analytical expression.

Neural networks provide a flexible and universal function approximator whose capacity can easily be modified by adding neurons or layers. Therefore, we write the parametric function $\xi_\theta(\mathbf{q})$ as neural network with n input and r output neurons. In particular, we use a network with two hidden layers and tanh activation functions

$$\xi_\theta(\mathbf{q}) = \mathbf{W}_{\text{out}} \tanh [\mathbf{W}_2 \tanh (\mathbf{W}_1 \begin{smallmatrix} \sin \\ \cos \end{smallmatrix}(\mathbf{q}) + \mathbf{b}_1) + \mathbf{b}_2] + \mathbf{b}_{\text{out}},$$

where tanh acts componentwisely and θ is the collection of all elements of \mathbf{W}_i and \mathbf{b}_i . The function $\begin{smallmatrix} \sin \\ \cos \end{smallmatrix} : \mathbb{R}^n \rightarrow \mathbb{R}^{2n}$ stacks the sines and cosines of the elements of the input vector. Using this transformation we implement the toroidal structure of the input space⁶. Fig. 15 visualizes the neural network model.

Differentiating the network output with respect to its input yields the Jacobian $\mathbf{J}_{\xi,\theta}(\mathbf{q}) = \frac{\partial \xi_\theta}{\partial \mathbf{q}}$. Further, the matrix $\mathbf{J}_{\xi,\theta}(\mathbf{q})$ can be differentiated with respect to the parameters θ . The expression $\frac{\partial \mathbf{J}_{\xi,\theta}(\mathbf{q})}{\partial \theta}$ describes the effect of the parameters θ on the Jacobian of the network. All the network parameters θ except the biases of the output layer have an effect on the Jacobian $\mathbf{J}_{\xi,\theta}(\mathbf{q})$.

Condition (5) is used to derive a scalar cost function that penalizes the cosine of the pairs $\nabla_{\mathbf{A}} h_i$ and $d\xi_{\theta,j}$. We write this in matrix-vector notation and introduce $\mathbf{v}_{x,i}^\top(\mathbf{q})$ being the i -th row in $\mathbf{J}_x(\mathbf{q})$ and $\mathbf{v}_{\xi,j}^\top(\mathbf{q})$ being the j -th row of $\mathbf{J}_{\xi,\theta}(\mathbf{q})$:

$$\begin{aligned} L(\mathbf{q}, \theta) &= \frac{\lambda_1}{2mr} \sum_{i=1}^m \sum_{j=1}^r \left(\frac{\mathbf{v}_{x,i}^\top \mathbf{A}^{-1} \mathbf{v}_{\xi,j}}{|\mathbf{A}^{-1} \mathbf{v}_{x,i}| \cdot |\mathbf{v}_{\xi,j}|} \right)^2 \\ &\quad + \frac{\lambda_2}{2 \binom{r}{2}} \sum_{i=1}^r \sum_{j=1}^r \left[\left(\frac{\mathbf{v}_{\xi,i}^\top \mathbf{A}^{-1} \mathbf{v}_{\xi,j}}{|\mathbf{A}^{-1} \mathbf{v}_{\xi,i}| \cdot |\mathbf{v}_{\xi,j}|} \right)^2 [i > j] \right], \end{aligned} \quad (24)$$

where $[i > j]$ denotes the Iverson bracket, which is 1 when the condition is true and 0 otherwise, and $\binom{n}{k}$ is the binomial coefficient. Notationally, we dropped the explicit dependence of \mathbf{q} and θ to remove some clutter from the equation.

The first part of the cost function penalizes the cosine between mutual rows of $\mathbf{J}_x \mathbf{A}^{-1}$ and $\mathbf{J}_{\xi,\theta}$, while the second part penalizes the cosine between two mutual rows of $\mathbf{J}_{\xi,\theta} \mathbf{A}^{-1}$ and $\mathbf{J}_{\xi,\theta}$. Those two terms can be weighted using the constants λ_1 and λ_2 . The second part of the cost function resembles the full-rank condition. By using the cosines of the angles between the gradients we assure that the magnitude of the gradients is not penalized. This is required, because the globally optimal solution would be $\xi(\mathbf{q}) = \text{const}$ otherwise.

We chose $\lambda_1 = 1000$ and $\lambda_2 = 1$, i.e., we assign much higher priority to the decoupling between task- and orthogonal coordinates than mutual decoupling between the orthogonal coordinates. Generally, when not allowing constant

⁶Within this paper we show results for robots with revolute joints only. However, the framework and the concepts are not restricted to purely revolute robots. The methods can also be used for robots having prismatic joints. In that case the sin and cos terms will be omitted for prismatic joints and the joint values will be directly fed to the first layer.

functions for $\xi_i(\mathbf{q})$, (24) cannot be optimized to zero. Consider for instance again the 3 DoF manipulator with 1 DoF task space. Then, optimizing (24) to zero would imply that we have found a triply orthogonal system. This, however, is only possible in exceptional cases for specific task foliations [BMS03, McK20]. Therefore, optimizing (24) will find a trade-off between the two terms. As we are more interested in the decoupling between task- and orthogonal coordinates we set λ_1 to a much higher value.

Then, suppose we have K samples \mathbf{q}_k of the selected subset of \mathcal{Q} . The total cost will be

$$L(\boldsymbol{\theta}) = \frac{1}{K} \sum_{k=1}^K L(\mathbf{q}_k, \boldsymbol{\theta}). \quad (25)$$

We sample the training data on the selected regions of the joint space $\bar{\mathcal{Q}}$.

Finally, gradient descent is performed on $L(\boldsymbol{\theta})$ using the ADAM algorithm [KB15]. Interestingly, the cost function is only dependent on the input-to-output Jacobian of the neural network. By construction the function $\xi_{\boldsymbol{\theta}}$ is always an integral of $\mathbf{J}_{\xi, \boldsymbol{\theta}}$, so we get the coordinate function $\xi_{\boldsymbol{\theta}}(\mathbf{q})$ for free when fitting the Jacobian $\mathbf{J}_{\xi, \boldsymbol{\theta}}(\mathbf{q})$ to the condition (5). The optimization simultaneously finds a set of vector fields as well as an integral of them.

The solution $\xi_{\boldsymbol{\theta}}(\mathbf{q})$ to (5) is by far not unique and will depend on the initialization of the parameters. After initialization, we optimize on the actual cost function (25). This can be interpreted as bending and warping the randomly initialized foliation.

The training procedure with the ADAM optimizer is carried out in multiple epochs consisting of multiple parameter update steps. In each epoch we sample new training data using a uniform distribution on \mathcal{Q} to prevent overfitting. For the implementation we use TensorFlow [AAB⁺16], which allows to evaluate analytical gradients and Jacobians of the neural network automatically and to generate fast code running on the GPU. We denote the optimized parameters by $\hat{\boldsymbol{\theta}}$ in the following.

6.1 Two Degrees of Freedom Example Revisited

Let us revisit the two degrees of freedom example from Sec. 5.1. The planar configuration space allows to visualize the results straightforwardly. We experienced that globally no smooth function $\xi(\mathbf{q})$ exists that creates a non-singular parametrization of the task induced foliation everywhere. This is because it involves parametrizing a 1-sphere with a single coordinate. Still, we train the model globally, i.e. we sample training data from the entire \mathcal{Q} and check how the network handles this issue.

We first fit the neural network using $\mathbf{A} = \mathbf{I}$ and evaluate isolines (orange) of the resulting coordinate function $\xi_{\hat{\boldsymbol{\theta}}}(\mathbf{q})$ in Fig. 16b. Isolines of the forward kinematics function $h(\mathbf{q})$ are shown in blue for reference. The background color of the plot encodes the angle between $\nabla_{\mathbf{A}} h$ and $d\xi$. If the background was white everywhere, the training would be optimal. However, as expected, there are certain regions where the model does not perform well, which are visualized by the colored regions in Fig. 16. We observe that each value exists twice on each self-motion manifold, as each isoline of $\xi(\mathbf{q})$ intersects each self-motion manifold twice. As expected we did not obtain a global coordinate function on the self-motion manifolds. Fig. 17b additionally shows the functions $h(\mathbf{q})$ and $\xi(\mathbf{q})$ as surface plot.

Fig. 16c shows the results for $\mathbf{A} = \mathbf{M}$. Similarly to the Euclidean case, the model performs well in large regions (white background color) and the function only parametrizes half of the self-motion manifolds uniquely.

Comparing the results obtained from training a coordinate function through a neural network and the numerical results from Sec. 5.1 shows some significant differences, but also similarities. Most importantly, we observe that the isolines of the trained function match the lines generated by the flow $\nabla_{\mathbf{A}} h$ to a large extent. However, the similarity becomes worse when reaching the attracting lines growing out of the equilibria. The trained coordinate function $\xi_{\hat{\boldsymbol{\theta}}}$ is, in contrast to the numerical results, smooth. Therefore, $\xi_{\hat{\boldsymbol{\theta}}}$ can never be a global chart of the self-motion manifolds, which we also observe in the results.

6.2 Non-Involutive Case

In the previous section we considered an example that also had an exact solution. We trained the function for orthogonal coordinates for the same model that we could also evaluate numerically. In contrast, we will consider now a model which has no numerical solution, i.e., the distribution of gradients of the task coordinates is non-involutive. In this case the numerical propagation of coordinates according to Sec. 5 fails, as the gradients of the task coordinates cannot be integrated to submanifolds of \mathcal{Q} .

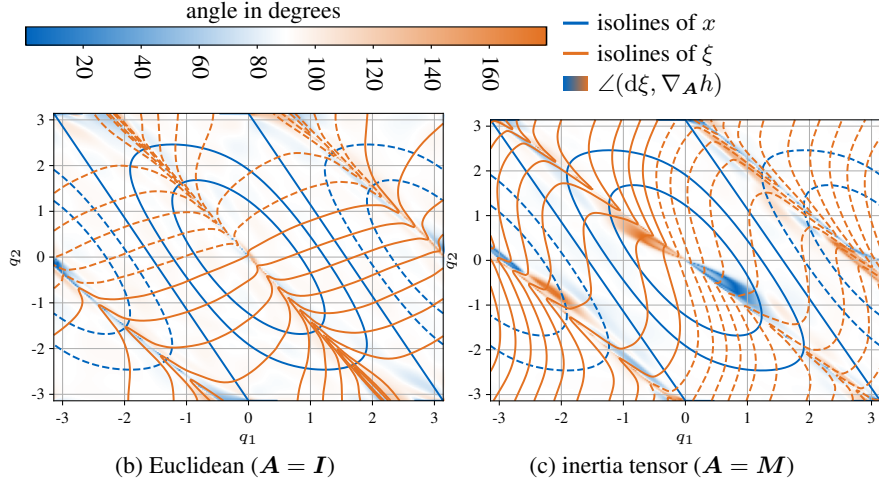


Figure 16: Resulting contour lines of the trained neural network for different metrics. The lines show isolines of the task coordinate x (blue) and quasi-orthogonal coordinate (ξ orange). Solid lines refer to positive values and dashed lines show negative isovalues. The background shows the local training accuracy.

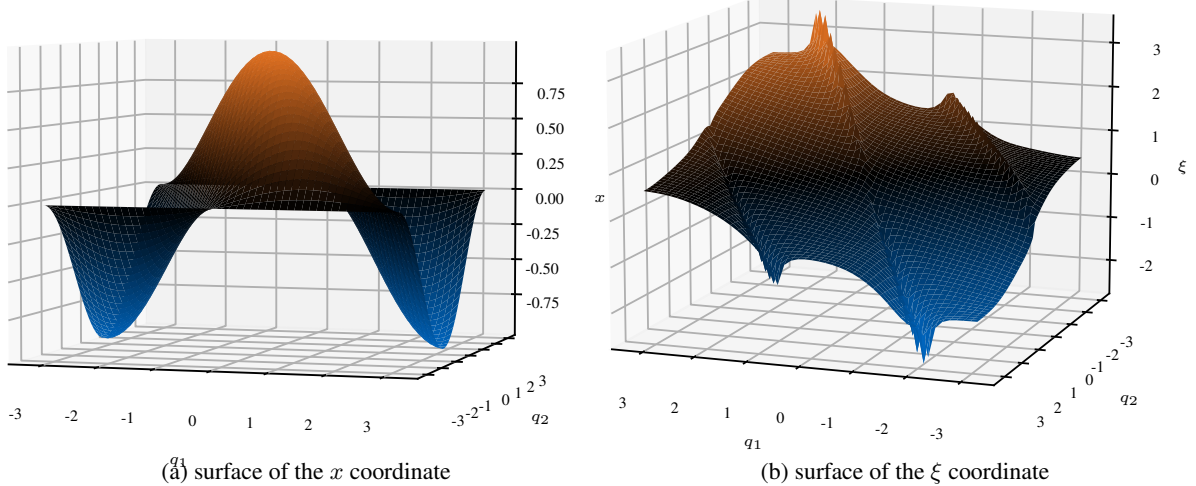


Figure 17: Surface plots of the the task coordinate function x (left) and the neural network approximation of a orthogonal coordinate ξ (right) for a two degrees of freedom manipulator for the Euclidean case ($A = I$).

Still, we can fit coordinate functions using the cost function (25) and aim at finding a ξ_θ which is *as orthogonal as possible*.

We consider again the manipulator with three degrees of freedom (Fig. 4b) and select both, the x - and y -component of the end effector position as task coordinates, i.e., $x = h_1(q)$ and $y = h_2(q)$. We therefore obtain a non-involutive system and train a neural network model using the cost function (25) as before.

The results are shown in Fig. 18 for a section of the configuration space. The blue lines show leaves of the task induced foliations, i.e., self-motion manifolds. Further, the red lines show $\nabla_I h_1$ and the green lines show $\nabla_I h_2$ scaled to unit length at that point, respectively. Each pair of $\nabla_I h_1$ and $\nabla_I h_2$ spans a plane visualized by the red rectangles. The planes belong to the distribution which we aim to integrate - an integral foliation for the distribution would have those planes as tangent planes. Finally, the gray surfaces correspond to isosurfaces of the foliation obtained by the learning process, i.e., surfaces on which $\xi(q)$ is constant, for three different values of $\xi(q)$. We observe that, despite the distribution not being involutive, the red planes are to a good approximation tangent to the isosurfaces.

In order to quantify the effect of the non-involutivity, we also train a neural model for an involutive case. This is achieved by removing the y -component of the end-effector position from the task coordinates, i.e., the task is only

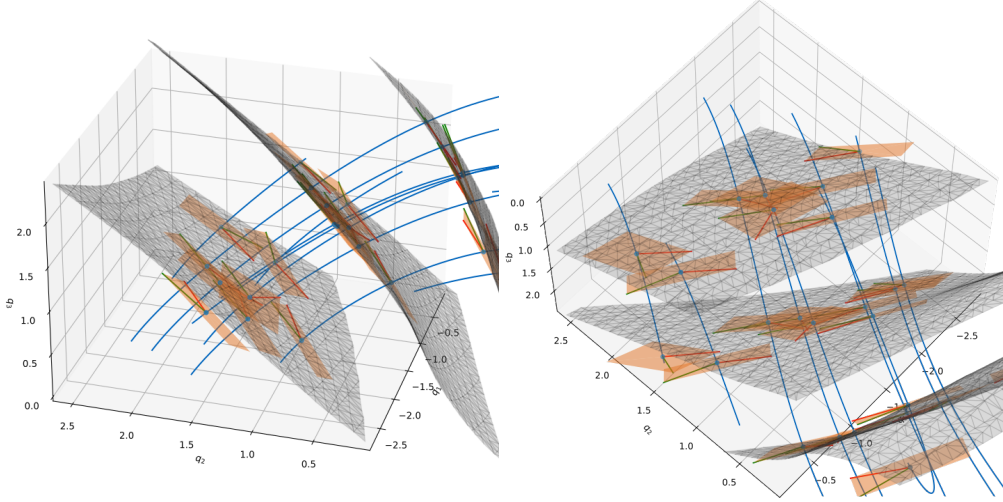


Figure 18: Results for a subset of the joint space of a three DoF robot with two task coordinates. The blue lines show leaves of the task induced foliation (self-motion manifolds) and the gray surfaces correspond to isosurfaces of the coordinate function the neural net found.

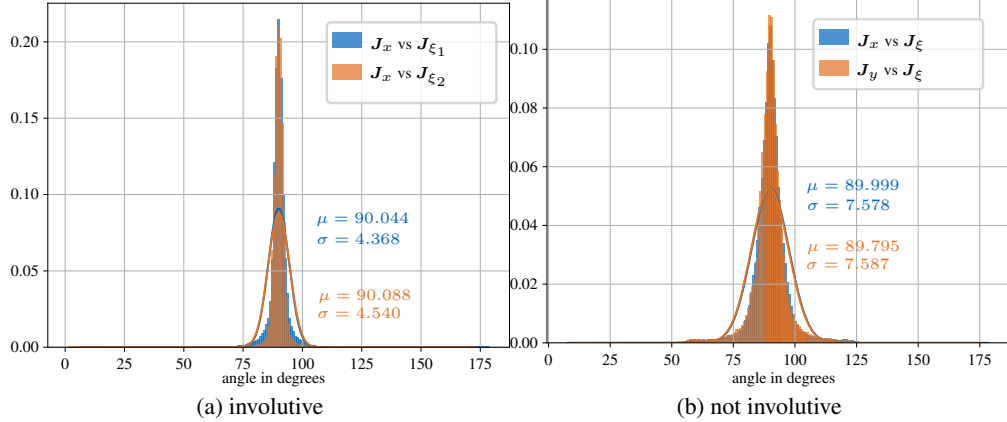


Figure 19: Histogram of angles between gradients of the task- and orthogonal coordinates for randomly sampled configurations for a trained neural network. On the left an involutive example is presented, while the right one is for a non-involutive example. The symbol μ denotes the mean and σ the standard deviation.

one-dimensional. We sample $N = 10^5$ joint configurations uniformly and compute the residual angle between the gradients. Fig. 19a shows the histogram of the residual angles between $d\xi_j$ and $\nabla_M h_i$. The results can be compared to the histogram in Fig. 19b, which shows the results for the non-involutive case. We observe that the histogram is, as expected, much more needle shaped in Fig. 19a than in Fig. 19b and the standard deviations of the angles are lower for the involutive case.

7 Controllers

To evaluate the applicability of the new orthogonal coordinates in simulation, we state well-known control approaches and show what the condition (5) implies for the closed-loop dynamics.

The standard rigid multi-body dynamics equation is used to model the manipulators

$$M(\mathbf{q})\ddot{\mathbf{q}} + \mathbf{C}(\mathbf{q}, \dot{\mathbf{q}})\dot{\mathbf{q}} + \mathbf{g}(\mathbf{q}) = \boldsymbol{\tau}. \quad (26)$$

7.1 Impedance Controller

As introduced in Sec. 3.2 we stack the task coordinates $\mathbf{x} = \mathbf{h}(\mathbf{q})$ and the (quasi-)orthogonal coordinates $\boldsymbol{\xi}(\mathbf{q})$ and obtain

$$\boldsymbol{\varphi}(\mathbf{q}) = \begin{bmatrix} \mathbf{h}(\mathbf{q}) \\ \boldsymbol{\xi}(\mathbf{q}) \end{bmatrix} \quad (27)$$

with the associated Jacobian (7) $\dot{\boldsymbol{\varphi}} = \mathbf{J}(\mathbf{q})\dot{\mathbf{q}}$. We use an impedance control law [Hog85]

$$\mathbf{f}_\varphi^{\text{imp}} = -\mathbf{K}_\varphi[\boldsymbol{\varphi}(\mathbf{q}) - \boldsymbol{\varphi}_d] - \mathbf{D}_\varphi \mathbf{J} \dot{\mathbf{q}}, \quad (28)$$

where $\boldsymbol{\varphi}_d$ denotes the desired position, \mathbf{K}_φ the desired stiffness and \mathbf{D}_φ the damping matrix. Given a diagonal matrix $\mathbf{Z} = \text{diag}(\zeta_1 \dots \zeta_m)$ of damping ratios, the damping matrix can be computed using the damping design equation [AOFH03]

$$\mathbf{D}_\varphi = \mathbf{M}_\varphi^{1/2} \mathbf{Z} \mathbf{K}_\varphi^{1/2} + \mathbf{K}_\varphi^{1/2} \mathbf{Z} \mathbf{M}_\varphi^{1/2}, \quad (29)$$

where $\mathbf{A}^{1/2}$ denotes the matrix-square root of \mathbf{A} such that $\mathbf{A} = \mathbf{A}^{1/2} \mathbf{A}^{1/2}$. The matrix \mathbf{M}_φ denotes the transformed mass matrix

$$\mathbf{M}_\varphi = (\mathbf{J} \mathbf{M}^{-1} \mathbf{J}^\top)^{-1}. \quad (30)$$

Suppose \mathbf{J}_x and \mathbf{J}_ξ are orthogonal with respect to the mass matrix, i.e., we have condition (5) for $\mathbf{A} = \mathbf{M}$ satisfied. One can easily verify that the term in the parenthesis of (30) will have block-diagonal structure (cf. [Kha95])

$$\begin{aligned} \mathbf{M}_\varphi^{-1} &= \mathbf{J} \mathbf{M}^{-1} \mathbf{J}^\top = \begin{bmatrix} \mathbf{J}_x \mathbf{M}^{-1} \mathbf{J}_x^\top & \mathbf{J}_x \mathbf{M}^{-1} \mathbf{J}_\xi^\top \\ \mathbf{J}_\xi \mathbf{M}^{-1} \mathbf{J}_x^\top & \mathbf{J}_\xi \mathbf{M}^{-1} \mathbf{J}_\xi^\top \end{bmatrix} \\ &= \begin{bmatrix} \mathbf{M}_x^{-1} & \mathbf{0} \\ \mathbf{0} & \mathbf{M}_\xi^{-1} \end{bmatrix}. \end{aligned} \quad (31)$$

Note that we notationally dropped the explicit dependency of \mathbf{J} , \mathbf{M} , \mathbf{D}_φ and \mathbf{M}_φ on \mathbf{q} to remove some clutter.

Using the transformation law for covectors we transform the resulting force from the impedance controller $\mathbf{f}_\varphi^{\text{imp}}$ to joint torques

$$\boldsymbol{\tau}_\varphi^{\text{imp}} = \mathbf{J}^\top \mathbf{f}_\varphi^{\text{imp}} \quad (32)$$

Suppose we apply the feedback control law

$$\boldsymbol{\tau}_1 = \mathbf{J}^\top \mathbf{f}_\varphi^{\text{imp}} + \mathbf{g}(\mathbf{q}) \quad (33)$$

on the multi-body dynamics (26) and let us solve for the acceleration $\ddot{\boldsymbol{\varphi}}$

$$\ddot{\boldsymbol{\varphi}} = \underbrace{\mathbf{J} \mathbf{M}^{-1} \mathbf{J}^\top}_{\mathbf{M}_\varphi^{-1}} \mathbf{f}_\varphi^{\text{imp}} + \underbrace{\dot{\mathbf{J}} \dot{\mathbf{q}}}_{\dot{\boldsymbol{\varphi}}_{\text{curv}}} - \underbrace{\mathbf{J} \mathbf{M}^{-1} \mathbf{C} \dot{\mathbf{q}}}_{\dot{\boldsymbol{\varphi}}_{\text{CC}}}. \quad (34)$$

The force due to the impedance controller $\mathbf{f}_\varphi^{\text{imp}}$ results in an acceleration $\ddot{\boldsymbol{\varphi}}$ via the block-diagonal mobility matrix \mathbf{M}_φ^{-1} (31). Therefore, the impedance controller will not create immediate accelerations in the task coordinates upon forces in the orthogonal coordinates and vice versa.

7.2 Trajectory Tracking

As derived above, the impedance controller will not create immediate disturbing accelerations between mutual sets of coordinates. It may, however, create delayed couplings via the accumulated velocity $\dot{\mathbf{q}}$. The joint velocity couples into the acceleration $\ddot{\boldsymbol{\varphi}}$ by the last two terms in (34): $\dot{\boldsymbol{\varphi}}_{\text{CC}}$, which expresses the task acceleration due to Coriolis and centrifugal forces and $\dot{\boldsymbol{\varphi}}_{\text{curv}}$, which depends on the curvature of the self-motion manifolds.

Consequently, in order to analyze the decoupling of the coordinates we need additional feed-forward terms. Assume a desired trajectory $(\boldsymbol{\varphi}_d(t), \dot{\boldsymbol{\varphi}}_d(t), \ddot{\boldsymbol{\varphi}}_d(t))$ for the task and the orthogonal coordinates. We then use the feed-forward controller

$$\mathbf{f}_\varphi^{\text{FF}} = \mathbf{M}_\varphi \left[\ddot{\boldsymbol{\varphi}}_d + \left(\mathbf{J} \mathbf{M}^{-1} \mathbf{C} - \dot{\mathbf{J}} \right) \mathbf{J}^{-1} \dot{\boldsymbol{\varphi}}_d \right] + \mathbf{D}_\varphi \dot{\boldsymbol{\varphi}}_d.$$

The resulting force is then transformed to joint torques using the covector transformation (32). The final control law is composed of the impedance controller (28) and the feed-forward terms

$$\boldsymbol{\tau}_2 = \mathbf{J}^\top [\mathbf{f}_\varphi^{\text{imp}} + \mathbf{f}_\varphi^{\text{FF}}] + \mathbf{g}(\mathbf{q}). \quad (35)$$

In (35) all the matrices are evaluated at the actual joint configuration. The control law is known as *operational space PD+ controller*.

The stability of the closed-loop system can be shown similar to [DWB⁺21, Sec. 3.2], where passivity and global asymptotic stability is shown for a joint space PD+ controller by deriving a storage function in joint coordinates. When writing the storage function in operational coordinates φ , the same reasoning as in [DWB⁺21] applies for the closed-loop system using (35). However, due to the existence of singularities in the coordinates, globality is lost and only local results are feasible.

8 Simulation

We use the three-DoF example manipulator (Fig. 4b) for the experimental validation of the orthogonal coordinates. For the dynamics we assume a mass of $m = 3$ for each link and assume the mass to be uniformly distributed over the link.

In order to employ the controller (35) a desired trajectory in terms of $(\varphi_d, \dot{\varphi}_d, \ddot{\varphi}_d)$ is required. We use a signal of pre-defined jumps $\dot{\varphi}(t)$ that we pass to a second-order low pass with natural frequency $\omega_0 = 2\pi$ and damping ratio $\zeta = 0.7$. This way, we obtain a twice-differentiable signal that can be used as desired trajectory. We simulate the dynamics of the system (26) in closed loop with the controllers using a Runge-Kutta integration scheme [HNW08].

8.1 Involutive Case

First, we show simulation results for the involutive case, i.e., one task coordinate and two orthogonal coordinates. We choose, as before, the x -component of the end-effector position as task coordinate. Consequently, we will have two orthogonal coordinates ξ_1 and ξ_2 .

We begin by showing simulation results using the linear, locally orthogonal coordinates (Sec. 4) and evaluate their performance and limitations. Afterwards we show simulation results using the neural network-based orthogonal coordinates and present how they overcome the limitations of the simple approach and also improve decoupling significantly. Finally, we also show results without the feed-forward controller and thus observe the behavior of the passive system with passive feedback. Additionally, we compare the contributions of different disturbing terms on the task acceleration and show that only a negligible contribution is due to inaccuracies in the orthogonal coordinates.

8.1.1 Plane Approximation

Two orthogonal coordinates ξ_1 and ξ_2 are required in this setting. Let $\mathbf{q}_0 \in \mathcal{Q}$ be the chosen base configuration for the locally orthogonal coordinates and consider the vector

$$\mathbf{v} = \nabla_{\mathbf{M}} \mathbf{h}(\mathbf{q}_0). \quad (36)$$

The vector \mathbf{v} must be contained in both planes for the orthogonal coordinates. We set

$$\mathbf{n}_1 = \frac{[v_2 \quad -v_1 \quad 0]^T}{\sqrt{v_1^2 + v_2^2}} \quad (37a)$$

$$\mathbf{n}_2 = \frac{\mathbf{n}_1 \times \mathbf{v}}{|\mathbf{n}_1 \times \mathbf{v}|} \quad (37b)$$

and use the base planes $E(\mathbf{q}_0, \mathbf{n}_1)$ and $E(\mathbf{q}_0, \mathbf{n}_2)$ for the linear, locally orthogonal coordinates (21). These locally orthogonal coordinates and the task coordinates are used in the trajectory tracking controller τ_2 (35). Two interleaved jumps in the x - and ξ_1 -coordinate are commanded. Fig. 20 shows the results for this experiment.

The initial configuration \mathbf{q}_0 is chosen such that the task self-motion manifolds shows comparatively low curvature and the base configuration for the orthogonal coordinates is set to the initial configuration. Even for relatively large motions in joint space (Fig. 20c) the dynamics of the task- and orthogonal coordinates, respectively, look moderately decoupled, which can be observed in the time-evolution of the coordinates and their desired values (Fig. 20a) as well as in Fig. 20b where the trajectory is projected onto the $x\xi_1$ -plane. Additionally, the decoupling performs better when the configuration is closer to the initial and base configuration \mathbf{q}_0 .

The first column of Fig. 22 (adgj) shows results for a longer simulation with multiple commanded jumps in all three coordinates for the same base configuration \mathbf{q}_0 . Fig. 22j shows the trajectory of the manipulator in joint space, where additionally the two relevant task self-motion manifolds are rendered. The self-motion manifolds show comparatively low curvature in this area.

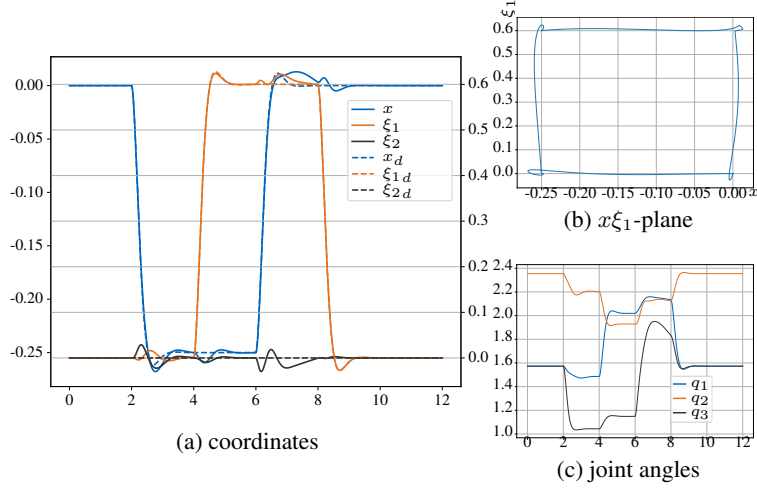


Figure 20: Results of dynamic simulation using the plane approximation $\xi_p(\mathbf{q})$ for interleaved steps in the x - and ξ_1 -coordinate.

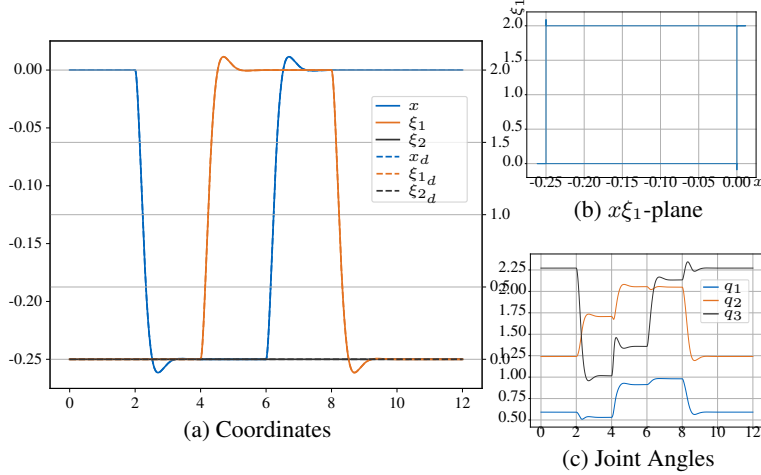


Figure 21: Results of dynamic simulation using the neural network model $\xi_{nn}(\mathbf{q})$ for interleaved steps in the x - and ξ_1 -coordinate.

However, for regions of larger curvature, the linear orthogonal coordinates do not perform well. The second column in Fig. 22 (behk) shows results for another initial configuration. Two major problems arise due to the curvature: (1) the decoupling is very poor and (2) the coordinates may contradict each other. Large cross-couplings between the coordinates on which the jump occurs and the other coordinates exist. Moreover, we observe that certain targets cannot be reached, which is due to the second problem of mutual contradiction of target values for the coordinates, i.e., task inconsistency.

8.1.2 Neural Network

Next, we take the neural network $\xi_{nn}(\mathbf{q})$ approximation trained for $\mathbf{A} = \mathbf{M}$. We use the same simulation and controller as before, we only replace the coordinate function $\xi_p(\mathbf{q})$ by the neural network $\xi_{nn}(\mathbf{q})$. We first repeat the same interleaved jumps as in Fig. 20. The results are shown in Fig. 21. Neither in the time evolution of the coordinates (Fig. 21a) nor in the trajectory plot (Fig. 21b) are any couplings observable. The overshoots are due to the damping ratio $\zeta = 0.7$ of the pre-filter for the trajectory generation.

The third column in Fig. 22 (cfil) shows again the experiment commanding jumps in all the coordinates. Also in this experiment we do not observe mutual coupling between the coordinates.

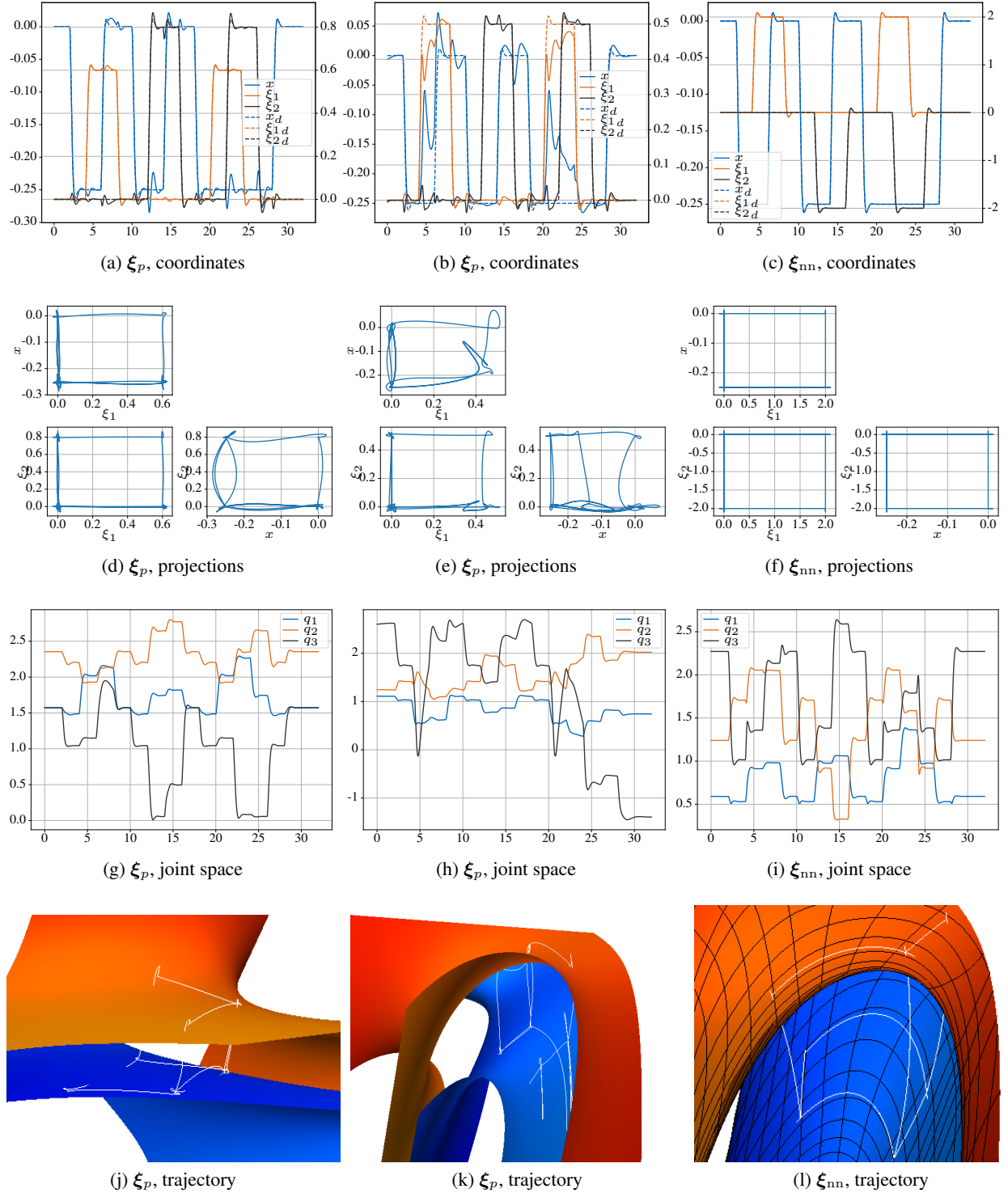


Figure 22: Simulation results for involutive case using the trajectory tracking controller for commanded jumps in the respective coordinates. While the first and middle columns show results for the simple linear, locally orthogonal coordinates ξ_p , the last column shows the results using ξ_{nn} . In the first row we show the time evolution of the desired- and actual values of the coordinates and in the second row we show the trajectory expressed in coordinates projected onto the coordinate planes. Comparison on the magnitude of the motion in joint space to ensure comparability can be read in the third row. Finally, the bottom row shows the trajectory of the manipulator in joint space rendered as the 3D-space curve. Additionally, the self-motion manifolds of the x -coordinates for the target values $x = 0$ and $x = 0.25$ are shown. For the neural network setting we also show the coordinate lines for ξ_1 and ξ_2 on the self-motion manifolds.

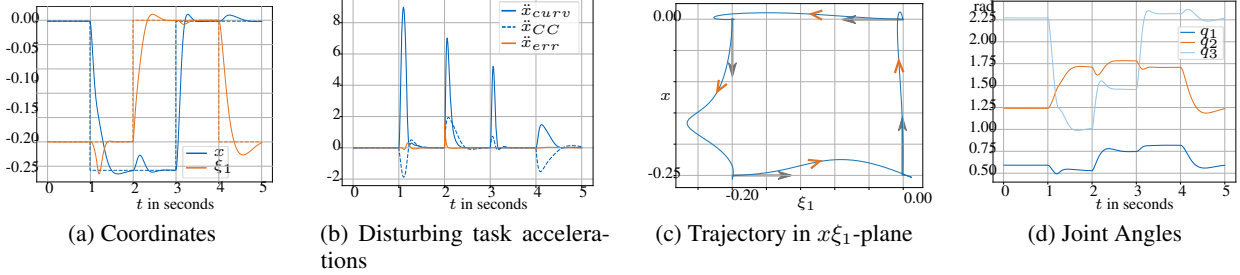


Figure 23: Simulation results with disabled feed-forward controller for interleaved jumps in the x - and ξ_1 -coordinate. (a): time evolution of the desired and actual value of the coordinates, (b): breakdown of the contribution to the disturbing unwanted task accelerations, (c) trajectory of the manipulator in coordinates projected onto the $x\xi_1$ -plane and (d): time evolution of the manipulator in joint space.

8.1.3 Feedback Only

We also show results for pure feedback control, i.e., we disable the feed-forward controller and only apply the feedback controller τ_1 (33). This way we can analyze the disturbing accelerations due to the curvature of the self-motion manifold and the Coriolis and centrifugal forces and compare them to the accelerations due to errors in the trained models. Further, we consider the case of regulation, i.e., $\dot{x}_d = \dot{\xi}_{i_d} = 0$.

For this experiment we use $\xi_{nn}(\mathbf{q})$ and command the same jumps as in Fig. 21 using the same initial configuration. Using the first row of (34) we compute the individual unwanted contributions to the task acceleration \ddot{x} . The term

$$\ddot{x}_{err} = \mathbf{J}_x \mathbf{M}^{-1} \mathbf{J}_\xi^\top \mathbf{f}_\xi^{\text{imp}} \quad (38)$$

denotes the contribution due to the training inaccuracies, i.e., if the desired condition (5) is satisfied this term will vanish. Fig. 23 shows the results. In contrast to the previous example including the feed-forward controller, now disturbances and couplings are clearly observable. However, when considering the breakdown of the individual contributions to the unwanted task acceleration in Fig. 23b, the model inaccuracies are very low compared to the other terms. In fact, we have negligible *immediate* task acceleration due to a force \mathbf{f}_ξ , but we observe delayed responses due to the accumulated speed generated by \mathbf{f}_ξ that couples in via the Coriolis- and centrifugal terms and the curvature of the self-motion manifolds.

8.2 Non-Involutive Case

For the non-involutive example we use the x - and y -coordinate as task coordinates and have only a single quasi-orthogonal coordinate ξ . The distribution Δ with the local basis $\{\nabla_M x, \nabla_M y\}$ is generally not involutive.

8.2.1 Plane Approximation

For the locally orthogonal coordinates we choose

$$\mathbf{n} = \frac{\nabla_M x(\mathbf{q}_0) \times \nabla_M y(\mathbf{q}_0)}{|\nabla_M x(\mathbf{q}_0) \times \nabla_M y(\mathbf{q}_0)|} \quad (39a)$$

$$\xi_p(\mathbf{q}) = \mathbf{n}^\top (\mathbf{q} - \mathbf{q}_0). \quad (39b)$$

Simulation results for interleaved jumps in the ξ - and x -coordinate are shown in Fig. 25 in the first two columns. We show the desired and actual values of the coordinates in the first row, the projection of the trajectory onto the $x\xi$ -plane in the middle row and the evolutions of joint angles on the bottom. We observe similar behavior as in the involutive example: for small jumps close to the base configuration \mathbf{q}_0 we get better decoupling, the decoupling becomes worse for larger step and we have the issue of contradicting targets for large jumps. The overall decoupling seems worse than in the involutive example, which is expected as the problem cannot have a perfect solution.

8.2.2 Neural Network

Next, we use $\xi_{nn}(\mathbf{q})$, where the network has been trained on the respective model. The last two columns of Fig 25 show the results of the simulation with ξ_{nn} . In comparison to the linear approximation with ξ_p the error is more distributed

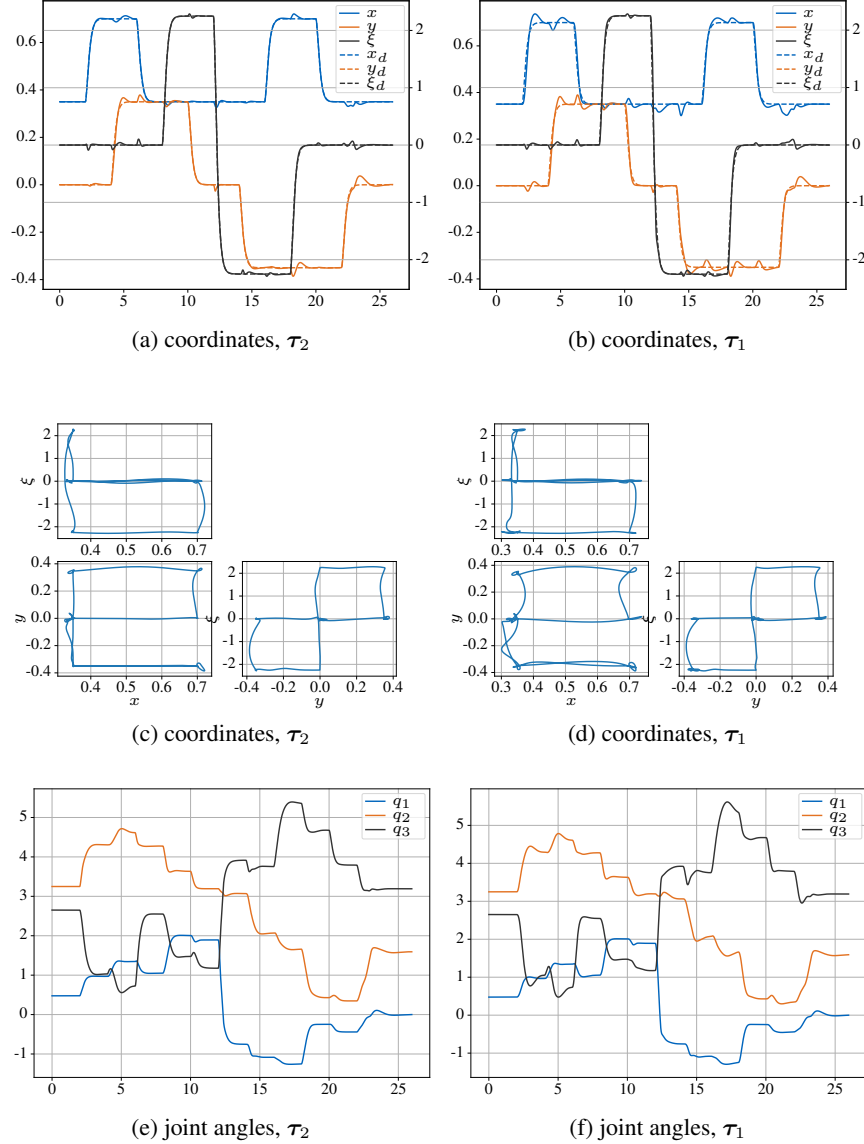


Figure 24: Additional simulation results for the non-involutive example. Left: trajectory tracking, right: impedance control.

over the space. While we have the best decoupling at q_0 for ξ_p , there is no priority to any points for the ξ_{nn} , so we have a better average approximation. The third column shows results with ξ_{nn} for large steps, i.e., we command jumps comparable to those where the linear model failed. Here, the neural network model still performs reasonably well.

Additionally, the fourth column shows the results for the same setting but with disabled feed-forward controller. In the experiments the observed coupling between the orthogonal coordinate ξ and the task coordinates was, as expected, less than the coupling between the mutual task coordinate x and y . This can also be observed in Fig. 25d.

Finally, Fig. 24 shows simulation results using ξ_{nn} command motion in all the coordinates with (first column) and without (second column) the feed-forward controller. Especially in the case without the feed-forward term we again observe larger coupling between x and y than between ξ and x/y .

In the non-involutive settings we cannot have perfect decoupling which is clearly observable when comparing the results to the involutive case. Especially, when comparing Figs. 22f and 24c the effect of the non-involutivity can be

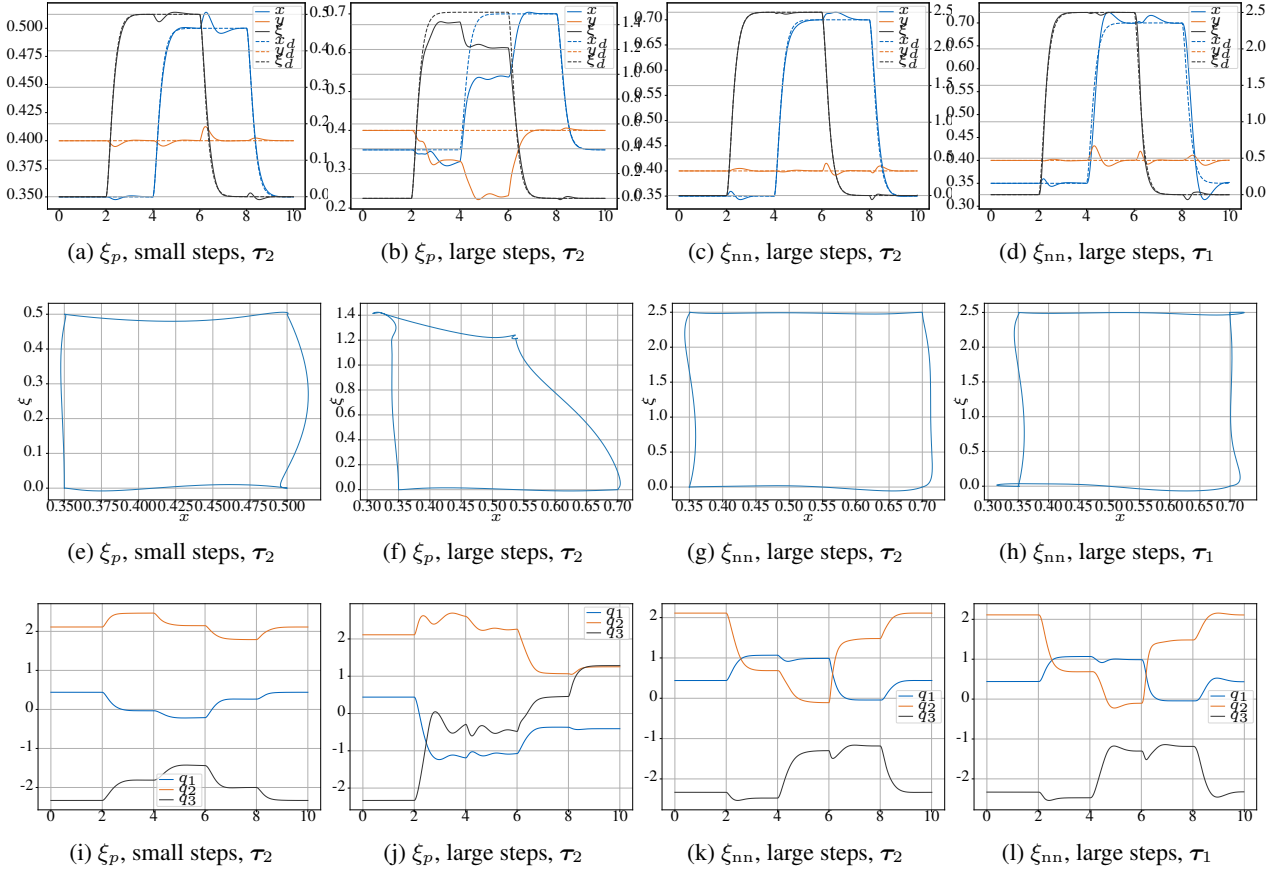


Figure 25: Simulation results for the non-involutive example for jumps in two of the coordinates. The first two columns show results using the linear, locally quasi-orthogonal coordinates ξ_p , the last two columns show results using ξ_{nn} .

observed. However, a decent performance can be achieved with this method even for large steps, in contrast to the linear locally orthogonal coordinates.

9 Discussion

In this paper we give, to our best knowledge, for the first time a systematic analysis of the geometrical aspects of robot redundancy resolution on configuration (position) level, i.e. in terms of quasi-orthogonal configuration space coordinates. The main conclusion is that exactly decoupled coordinates can in general only be achieved if the task space is one-dimensional. For higher dimensions, this is only possible in particular cases of forward kinematics, as shown in [McK20, pp. 151–154] for three dimensions. For all other cases we introduced the concept of quasi-orthogonal coordinates, providing the best possible decoupling in a certain least mean squares sense. One might ask, beyond the quite exciting geometric insights on the problem, what are the practical advantages of this new approach for robotics? While it is too early to draw general conclusions, some obvious aspects can be already discussed.

9.1 What does decoupling on position-level imply?

The classical impedance control approaches [Kha87, DWAH12, SK05] use on all priority levels but the highest ones coordinates $\psi(\mathbf{q})$ which may conflict with the top level coordinates in general. The generalized force projected to the second priority level in (3b) usually is the partial derivative of a potential function $U_\psi(\psi(\mathbf{q}))$ defined in these coordinates

$$\mathbf{f}_2^\top = \frac{\partial U_\psi(\psi(\mathbf{q}))}{\partial \mathbf{q}}. \quad (40)$$

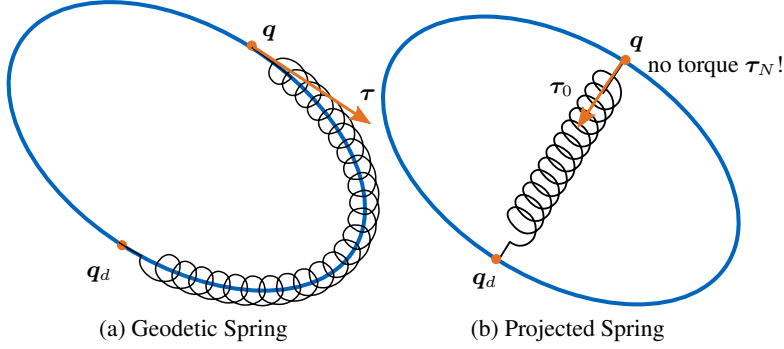


Figure 26: Comparison of a geodetic spring due to the position-level redundancy resolution approach in this paper and a projected spring by the state of the art approach (b). The spring in (b) has no effect as the joint torques vanish after the projection. The blue ellipses sketch a task self-motion manifold.

For admittance type controllers similar potentials or distance functions are used, with the difference that the forces are transformed to velocity commands on task level and the projection is then done on the velocity level as in (1b). This approach has two major implications:

- Local extrema exist, i.e., one can have non-zero torques $\tau = \mathbf{J}_\psi^\top \mathbf{f}_2 \neq 0$ which vanish after the projection, such that $\mathbf{P}^\top \mathbf{J}_\psi^\top \mathbf{f}_2 = 0$. Fig. 26b sketches this situation for a joint space spring. For lower priority springs, only those torque components tangent to the self-motion manifolds⁷ survive the projection. Such a projected force will have no effect if it only has components normal to the self-motion manifold. This may lead to highly tensioned springs with a lot of stored energy hidden behind the projections. Small variations of the configurations or of the commanded motions may cause the previously hidden spring to suddenly discharge and create large forces. In contrast, (quasi-) orthogonal coordinates allow the definition of *geodetic springs*, directly depending on the distance between the two end-points on the self-motion manifolds (Fig. 26a).
- Through the projection, the potential is actually altered, making a simple passivity based analysis for the multi-priority impedance control impossible⁸. Using advanced control theoretic analysis, the proof of controller convergence in the case for a unique equilibrium of all potentials has been achieved both velocity and torque level redundancy resolution, for the regulation and for the tracking case [Ant09, ODAS15, DO20]. However, the complexity of the proofs also reflects the intrinsic difficulty introduced by the projection of potentials and springs.

The above mentioned problems vanish in the case of orthogonal coordinates, in which no projection is needed and convergence analysis can be done simply based on the sum of all potentials. In the quasi-orthogonal coordinates case, the problems are substantially reduced from practical perspective, as demonstrated by the simulation examples. They still persist from theoretical viewpoint. Note, however, that in this case, an additional projection can always still be applied. One can use the projectors \mathbf{P} or \mathbf{P}^\top on the quasi-orthogonal foliations to remove remaining couplings. In contrast to the classical approach, the projection will only remove a very small portion of the velocity $\dot{\mathbf{q}} = \mathbf{J}_\xi^\# \dot{\xi}$ or force $\tau = \mathbf{J}_\xi^\top \mathbf{f}_\xi$.

Of course, further experiments need to verify under which circumstances the additional effort of learning quasi-orthogonal coordinates in addition to the classical projections is justified in practice.

The three robot examples treated in the current paper exemplify essential theoretical questions raised by finding orthogonal coordinates, addressing both multi-dimensional task spaces and multi-dimensional self-motion manifolds. In this way, both an involutive and and non-involutive distribution case have been addressed. Higher dimensional configuration spaces would not add substantially to the theoretical discussion. However, from practical perspective, it remains open how the learning and the behavior of the quasi-orthogonal coordinates scale with dimensionality of the configuration space. Further work will therefore need to answer the question of applicability of the approach to redundant robots such as seven DoF arms or humanoids.

⁷When using the dynamically consistent projector actually those components in the null space of $\mathbf{M}^{-1} \mathbf{J}_x$ remain as these accelerate the system tangent to the self-motion manifolds. Without loss of generality, we stick to the Euclidean case above as it is easier to explain and visualize.

⁸Unless also feeding back the external forces in the controller [DWB⁺17].

9.2 Motion Planning

Besides the relevance for impedance control or for redundancy resolution on velocity level, the quasi-orthogonal foliations approach might be of major relevance to motion planning as well. Indeed, in practical applications, desired trajectories for the hierarchical impedance controllers still are provided by motion planners which operate in the very high-dimensional configuration space of the robots. Therefore, online motion planning and re-planning still is a time-critical aspect of real-time robot operation. The new concept of orthogonal foliations allows a quite precise lower-dimensional representation of the search space for the lower priority tasks. The learning of the quasi-orthogonal coordinates related to a given task space can be done offline, considerably reducing the dimensionality of the online planning problem.

9.3 Representation of Orthogonal Foliations

The objective of finding orthogonal foliations can be written as a system of partial differential equations.

In this paper we have done a proof of concept for the orthogonal foliations and have formulated the objective as optimization problem. We then have chosen a neural network model and fitted it to the formulated cost function. Probably, a variety of other solutions to find a $\xi(q)$ optimally satisfying (5) exist. For instance, discrete methods and finite elements are often used in the field of computer vision and computer graphics, mechanical and structure analysis and materials science to solve PDEs.

The approximation by linear local quasi-orthogonal coordinates, which we employed for comparison in the experiments, might provide a practical value by itself. If one considers the learning of quasi-orthogonal coordinates too expensive, one could still use the linear approximation in combination with classical projection based methods instead of defining potentials classically, directly in joint space. One can expect in practice that the components which need to be projected out will be substantially reduced. To our knowledge, this approach has also not been published before.

The comparison and detailed investigation of different approaches to find a parametrization $\xi(q)$ for quasi-orthogonal foliations based on (5) was not within the scope of this paper and will be addressed in future work.

10 Conclusions

This paper developed a first approach for redundancy resolution on position level. Given an n degree of freedom robot with m -dimensional task we create additional $n-m$ coordinate functions in order to fully specify the system. The desired property of the additional coordinates is to be decoupled from the task coordinates with respect to the dynamics of the robot. Basically, the Jacobian of the additional coordinates resembles the conditions known from state of the art velocity based redundancy resolution. Exact decoupling can, however, only be achieved when the distribution of the gradients of the task coordinates is involutive. Unfortunately, this is a rare special case and that is rarely fulfilled. We therefore formulate an optimization problem and strive for as little as possible coupling between task and additional coordinates. We call the additional coordinates *orthogonal foliations*.

As a first step we used a neural network as model function that was trained to satisfy the desired condition on its Jacobian as well as possible. Alternative solutions to find orthogonal foliations are an open question and require future work.

We used the neural network based orthogonal foliations and achieved very good decoupling in the involutive and decent decoupling in the non-involutive case. No projection was used for the experiments. Therefore, we could observe that decoupling at position level was achieved to a large extent.

In our opinion the position-level redundancy resolution provides a very interesting approach compared to the state of the art velocity-level decoupling. Additionally, the foliation-view on classical forward kinematics provides insight to the global behavior of robot kinematics.

Acknowledgements

The authors would like to thank Daniel Matthes from the TU Munich for initial discussions and literature hints on the topic and to Benjamin McKay from the University College Cork for his feedback on triply orthogonal webs and foliations and for addressing one of our main questions in his manuscript [McK20, pp. 151–154]. Special thanks are also directed to Alexander Dietrich from the DLR for a general revision of this paper.

Funding

This work is supported by the Advanced Grant M-Runners (ID: 835284) by the European Research Council (ERC).

Appendix

Discrete Harmonic Functions on Curved Manifolds

The algorithm below is according to [BKP⁺10, Pau18]. Let v_i denote the i -th vertex of the mesh. Let $\mathcal{N}_1(v_i)$ denote the one-ring neighborhood of the i -th vertex. Let $\partial\mathcal{S}$ denote the (discrete) boundary of the mesh, i.e. all vertices which are on the boundary.

We solve the linear system

$$\mathbf{L}\mathbf{u} = \mathbf{b}, \quad (41)$$

where \mathbf{L} and \mathbf{b} are sparse matrices created by

$$\mathbf{L}_{ij} = \begin{cases} 1, & \text{if } i = j \text{ and } v_i \in \partial\mathcal{S}, \\ \omega_{ij}, & \text{if } v_j \in \mathcal{N}_1(v_i), \\ -\sum_{v_j \in \mathcal{N}_1(v_i)} \omega_{ij}, & \text{if } i = j \text{ and } v_i \notin \partial\mathcal{S}, \\ 0, & \text{otherwise.} \end{cases} \quad (42)$$

$$\mathbf{b}_{ij} = \begin{cases} x_i, & \text{if } v_i \in \partial\mathcal{S} \text{ and } j = 1, \\ y_i, & \text{if } v_i \in \partial\mathcal{S} \text{ and } j = 2, \\ 0, & \text{otherwise.} \end{cases} \quad (43)$$

The x_i and y_i are the predefined targets for the boundary vertices. Here, we map the boundary $\partial\mathcal{S}$ to the unit-circle and set x_i and y_i accordingly.

In (42) weights ω_{ij} are

$$\omega_{ij} = \cot \alpha_{ij} + \cot \beta_{ij}, \quad (44)$$

where α_{ij} and β_{ij} are the two angles opposite to the edge e_{ij} from vertex v_i to v_j . The discrete bijective embedding can then be compute by solving (41) for \mathbf{u} .

References

- [AAB⁺16] Martín Abadi, Ashish Agarwal, Paul Barham, Eugene Brevdo, Zhifeng Chen, Craig Citro, Greg S. Corrado, Andy Davis, Jeffrey Dean, Matthieu Devin, Sanjay Ghemawat, Ian Goodfellow, Andrew Harp, Geoffrey Irving, Michael Isard, Yangqing Jia, Rafal Jozefowicz, Lukasz Kaiser, Manjunath Kudlur, Josh Levenberg, Dandelion Mané, Rajat Monga, Sherry Moore, Derek Murray, Chris Olah, Mike Schuster, Jonathon Shlens, Benoit Steiner, Ilya Sutskever, Kunal Talwar, Paul Tucker, Vincent Vanhoucke, Vijay Vasudevan, Fernanda Viégas, Oriol Vinyals, Pete Warden, Martin Wattenberg, Martin Wicke, Yuan Yu, and Xiaoqiang Zheng. TensorFlow: Large-scale machine learning on heterogeneous systems. In *Proceedings of the USENIX Symposium on Operating Systems Desgin and Implementation (OSDI)*, volume 12, pages 265–283, Savannah, GA, USA, November 2016.
- [Ant09] Gianluca Antonelli. Stability analysis for prioritized closed-loop inverse kinematic algorithms for redundant robotic systems. *IEEE Transactions on Robotics*, 25(5):985–994, 2009.
- [AOFH03] Alin Albu-Schäffer, Christian Ott, Udo Frese, and Gerd Hirzinger. Cartesian impedance control of redundant robots: recent results with the DLR-light-weight-arms. In *Proceedings of the IEEE International Conference on Robotics and Automation*, volume 3, pages 3704–3709, September 2003.
- [BB98] P. Baerlocher and R. Boulic. Task-priority formulations for the kinematic control of highly redundant articulated structures. In *Proceedings of the IEEE/RSJ International Conference on Intelligent Robots and Systems. Innovations in Theory, Practice and Applications*, volume 1, pages 323–329 vol.1, 1998.
- [BCG⁺91] Robert L. Bryant, S. S. Chern, Robert B. Gardner, Hubert L. Goldschmidt, and P. A. Griffiths. *Exterior Differential Systems*. Springer, New York, NY, 1991.
- [BGG03] Robert L. Bryant, Phillip A. Griffiths, and Daniel A. Grossman. *Exterior Differential Systems and Euler-Lagrange Partial Differential Equations*. University of Chicago Press, 2003.

[BKP⁺10] Mario Botsch, Leif Kobbelt, Mark Pauly, Pierre Alliez, and Bruno Lévy. *Polygon Mesh Processing*. AK Peters/CRC Press, 2010.

[BMS03] Alexander. I. Bobenko, Daniel Matthes, and Yuri B. Suris. Discrete and smooth orthogonal systems: C^∞ -approximation. *International Mathematics Research Notices*, 2003(45):2415–2459, January 2003.

[Bur89] Joel W. Burdick. On the inverse kinematics of redundant manipulators: characterization of the self-motion manifolds. In *Proceedings of the IEEE International Conference on Robotics and Automation*, pages 264–270. IEEE Computer Society, 1989.

[Cho45] Gustave Choquet. Sur un type de transformation analytique généralisant la représentation conforme et définie au moyen de fonctions harmoniques. *Bulletin des Sciences Mathématiques*, 69:156–165, 1945.

[DCGP19] Loris Di Cairano, Matteo Gori, and Marco Pettini. Coherent Riemannian-geometric description of Hamiltonian order and chaos with Jacobi metric. *Chaos: An Interdisciplinary Journal of Nonlinear Science*, 29(12):123134, 2019.

[DMB93] Keith L. Doty, Claudio Melchiorri, and Claudio Bonivento. A theory of generalized inverses applied to robotics. *The International Journal of Robotics Research*, 12(1):1–19, 1993.

[DO20] A. Dietrich and C. Ott. Hierarchical impedance-based tracking control of kinematically redundant robots. *IEEE Transactions on Robotics*, 36(1):204–221, 2020.

[DOAS13] Alexander Dietrich, Christian Ott, and Alin Albu-Schäffer. Multi-objective compliance control of redundant manipulators: Hierarchy, control, and stability. In *Proceedings of the IEEE/RSJ International Conference on Intelligent Robots and Systems*, pages 3043–3050, November 2013.

[DOAS15] Alexander Dietrich, Christian Ott, and Alin Albu-Schäffer. An overview of null space projections for redundant, torque-controlled robots. *The International Journal of Robotics Research*, 34(11):1385–1400, 2015.

[DWAH12] Alexander Dietrich, Thomas Wimböck, Alin Albu-Schäffer, and Gerd Hirzinger. Integration of reactive, torque-based self-collision avoidance into a task hierarchy. *IEEE Transactions on Robotics*, 28(6):1278–1293, December 2012.

[DWB⁺17] Alexander Dietrich, Xuwei Wu, Kristin Bussmann, Christian Ott, Alin Albu-Schäffer, and Stefano Stramigioli. Passive hierarchical impedance control via energy tanks. *IEEE Robotics and Automation Letters*, 2(2):522–529, 2017.

[DWB⁺21] Alexander Dietrich, Xuwei Wu, Kristin Bussmann, Marie Harder, Maged Iskandar, Johannes Englsberger, Christian Ott, and Alin Albu-Schäffer. Practical consequences of inertia shaping for interaction and tracking in robot control. *Control Engineering Practice*, 114:104875, 2021.

[FH05] Michael S. Floater and Kai Hormann. Surface parameterization: a tutorial and survey. In Neil A. Dodgson, Michael S. Floater, and Malcolm A. Sabin, editors, *Advances in Multiresolution for Geometric Modelling*, pages 157–186, Berlin, Heidelberg, 2005. Springer Berlin Heidelberg.

[Fro77] G. Frobenius. Über das Pfaffsche Problem. *Journal für die reine und angewandte Mathematik*, 82:230–315, 1877.

[HK87] John Hollerbach and Ki C. Suh. Redundancy resolution of manipulators through torque optimization. *IEEE Journal on Robotics and Automation*, 3(4):308–316, August 1987.

[HKT⁺09] Ulrich Hagn, Rainer Konietschke, Andreas Tobergte, Mathias Nickl, Stefan Jörg, Bernhard Kübler, Georg Passig, Martin Gröger, Florian Fröhlich, Ulrich Seibold, Luc Le-Tien, Alin Albu-Schäffer, Alexander Nothelfer, Franz Hacker, Markus Grebenstein, and Gerd Hirzinger. DLR MiroSurge - a versatile system for research in endoscopic telesurgery. *International Journal of Computer Assisted Radiology and Surgery*, Volume:183–193, 2009.

[HNW08] Ernst Hairer, Syvert P. Nørsett, and Gerhard Wanner. *Solving Ordinary Differential Equations I: Nonstiff Problems*. Springer Berlin Heidelberg, 2008.

[Hog85] Neville Hogan. Impedance control: An approach to manipulation: Part I-Theory; Part II-Implementation; Part III-Applications. *Journal of Dynamic Systems, Measurement and Control*, 107(1):1–24, 1985.

[HOW14] Jessica Hutzl, David Oertel, and Heinz Wörn. Knowledge-based direction prediction to optimize the null-space parameter of a redundant robot in a telemanipulation scenario. In *IEEE International Symposium on Robotic and Sensors Environments (ROSE) Proceedings*, pages 25–30, October 2014.

[KB15] Diederik P. Kingma and Jimmy Ba. Adam: A method for stochastic optimization. In Yoshua Bengio and Yann LeCun, editors, *International Conference on Learning Representations*, 2015.

[KH83] Charles A. Klein and Ching-Hsiang Huang. Review of pseudoinverse control for use with kinematically redundant manipulators. *IEEE Transactions on Systems, Man, and Cybernetics*, 13(2):245–250, March 1983.

[Kha85] Oussama Khatib. Real-time obstacle avoidance for manipulators and mobile robots. In *Proceedings of the IEEE International Conference on Robotics and Automation*, volume 2, pages 500–505, March 1985.

[Kha87] Oussama Khatib. A unified approach for motion and force control of robot manipulators: The operational space formulation. *IEEE Journal on Robotics and Automation*, 3(1):43–53, 1987.

[Kha95] Oussama Khatib. Inertial properties in robotic manipulation: An object-level framework. *The International Journal of Robotics Research*, 14(1):19–36, 1995.

[Kne26] Hellmuth Kneser. Lösung der aufgabe 41. *Jahresbericht der Deutschen Mathematiker-Vereinigung*, 35:116–124, 1926.

[LC87] William E. Lorensen and Harvey E. Cline. Marching cubes: A high resolution 3d surface construction algorithm. *SIGGRAPH Comput. Graph.*, 21(4):163–169, August 1987.

[Lee12] John M Lee. *Introduction to Smooth Manifolds*. Graduate Texts in Mathematics. Springer New York, second edition, 2012.

[LLVT03] Thomas Lewiner, Hélio Lopes, Antônio Wilson Vieira, and Geovan Tavares. Efficient implementation of marching cubes cases with topological guarantees. *Journal of Graphics Tools*, 8(2):1–15, December 2003.

[LP17] Kevin M. Lynch and Frank C. Park. *Modern Robotics: Mechanics, Planning, and Control*. Cambridge University Press, New York, NY, USA, 1st edition, 2017.

[McK20] Benjamin McKay. Introduction to exterior differential systems, September 2020.

[MDV⁺17] Nico Mansfeld, Badis Djellab, Jaime Raldua Veuthey, Fabian Beck, and Sami Haddadin. Improving the performance of biomechanically safe velocity control for redundant robots through reflected mass minimization. In *Proceedings of the IEEE/RSJ International Conference on Intelligent Robots and Systems*, 2017.

[MIH91] Ferdinando A. Mussa-Ivaldi and Neville Hogan. Integrable solutions of kinematic redundancy via impedance control. *The International Journal of Robotics Research*, 10(5):481–491, 1991.

[MK85] Anthony A. Maciejewski and Charles A. Klein. Obstacle avoidance for kinematically redundant manipulators in dynamically varying environments. *The International Journal of Robotics Research*, 4(3):109–117, 1985.

[MM99] S. Maneewongvatana and Dave Mount. It’s okay to be skinny, if your friends are fat. *Center for Geometric Computing 4th Annual Workshop on Computational Geometry*, 1999.

[MSZ94] Richard M. Murray, S. Shankar Sastry, and Li Zexiang. *A Mathematical Introduction to Robotic Manipulation*. CRC Press, Inc., Boca Raton, FL, USA, 1st edition, 1994.

[NCM⁺08] Jun Nakanishi, Rick Cory, Michael Mistry, Jan Peters, and Stefan Schaal. Operational space control: A theoretical and empirical comparison. *The International Journal of Robotics Research*, 27(6):737–757, 2008.

[NHY87] Yoshihiko Nakamura, Hideo Hanafusa, and Tsuneo Yoshikawa. Task-priority based redundancy control of robot manipulators. *The International Journal of Robotics Research*, 6(2):3–15, 1987.

[ODAS15] Christian Ott, Alexander Dietrich, and Alin Albu-Schäffer. Prioritized multi-task compliance control of redundant manipulators. *Automatica*, 53:416–423, 2015.

[OKN08] C. Ott, A. Kugi, and Yoshihiko Nakamura. Resolving the problem of non-integrability of nullspace velocities for compliance control of redundant manipulators by using semi-definite lyapunov functions. In *IEEE International Conference on Robotics and Automation*, pages 1999–2004, 2008.

[Pau18] Mark Pauly. Digital 3d geometry processing. Course at Ecole Polytechnique Fédérale de Lausanne (EPFL), 2018.

[PBP95] F.C. Park, J.E. Bobrow, and S.R. Ploen. A lie group formulation of robot dynamics. *The International Journal of Robotics Research*, 14(6):609–618, 1995.

[PCY99] J. Park, W. Chung, and Y. Youm. On dynamical decoupling of kinematically redundant manipulators. In *Proceedings of the IEEE/RSJ International Conference on Intelligent Robots and Systems. Human and Environment Friendly Robots with High Intelligence and Emotional Quotients*, volume 3, pages 1495–1500 vol.3, 1999.

[PK98] Frank Chongwoo Park and Jin Wook Kim. Manipulability and singularity analysis of multiple robot systems: a geometric approach. In *Proceedings of the IEEE International Conference on Robotics and Automation*, volume 2, pages 1032–1037, 1998.

[Rad26] Tibor Radó. Aufgabe 41. *Jahresbericht der Deutschen Mathematiker-Vereinigung*, 35:49, 1926.

[SA01] Wade Ramey Sheldon Axler, Paul Bourdon. *Harmonic Function Theory*. Springer, New York, NY, 2001.

[Sel96] Jonathan M. Selig. *Geometric Fundamentals of Robotics*. Monographs in Computer Science. Springer Science+Business Media New York, 1996.

[SG08] Jorge Sotomayor and Ronaldo Garcia. Lines of curvature on surfaces, historical comments and recent developments. *The São Paulo Journal of Mathematical Sciences*, 2(1):99–139, June 2008.

[SHV05] Mark W. Spong, Seth Hutchinson, and M. Vidyasagar. *Robot Modeling and Control*. Wiley, 2005.

[Sic90] Bruno Siciliano. Kinematic control of redundant robot manipulators: A tutorial. *Journal of Intelligent and Robotic Systems*, 3:201–212, September 1990.

[SK05] Luis Sentis and Oussama Khatib. Synthesis of whole-body behaviors through hierarchical control of behavioral primitives. *International Journal of Humanoid Robotics*, 02(04):505–518, 2005.

[SK08] B. Siciliano and O. Khatib, editors. *Springer Handbook of Robotics*. Springer Berlin Heidelberg, 2008.

[SLM⁺19] Hang Su, Shuai Li, Jagadeesh Manivannan, Luca Bascetta, Giancarlo Ferrigno, and Elena De Momi. Manipulability optimization control of a serial redundant robot for robot-assisted minimally invasive surgery. In *Proceedings of the International Conference on Robotics and Automation (ICRA)*, pages 1323–1328, May 2019.

[SS91] B. Siciliano and J.-J.E. Slotine. A general framework for managing multiple tasks in highly redundant robotic systems. In *Fifth International Conference on Advanced Robotics 'Robots in Unstructured Environments*, pages 1211–1216 vol.2, 1991.

[SSVO09] Bruno Siciliano, Lorenzo Sciavicco, Luigi Villani, and Giuseppe Oriolo. *Robotics: Modelling, Planning and Control*. Springer Publishing Company, Incorporated, London, 1st edition, 2009.

[SW15] Gerald Jay Sussman and Jack Wisdom. *Structure and Interpretation of Classical Mechanics, Second Edition*. The MIT Press, Cambridge, MA, USA, 2015.

[Wal90] Ian D. Walker. The use of kinematic redundancy in reducing impact and contact effects in manipulation. In *Proceedings of the IEEE International Conference on Robotics and Automation*, volume 1, pages 434–439, May 1990.